

DETERMINING THE ROLE OF FRACTAL GEOMETRY AND FRACTURE ENERGY IN  
BRITTLE BILAYER MATERIALS

By

ROBERT LEE SMITH

A DISSERTATION PRESENTED TO THE GRADUATE SCHOOL  
OF THE UNIVERSITY OF FLORIDA IN PARTIAL FULFILLMENT  
OF THE REQUIREMENTS FOR THE DEGREE OF  
DOCTOR OF PHILOSOPHY

UNIVERSITY OF FLORIDA

2009

© 2009 Robert Lee Smith

To my parents for all of their help and support

## ACKNOWLEDGMENTS

I thank Dr. Mecholsky for his guidance and understanding during my time at the University of Florida. I have learned much about materials science, and life in general, under his guidance and tutorage.

I thank the other members of my supervisory committee, Dr. Anthony Brennan, Dr. Wolfgang Sigmund, Dr. Laurie Gower, and Dr. Bhavani Sankar, for their advice and input while working on my dissertation project. I would especially like to thank Dr. Anthony Brennan for the discussions that we had that helped me gain a better understanding of my work.

I want to thank my colleague, Dr. Chuchai Anunmana, for making all of the specimens that I used in my project, for the flexure testing of the specimens, and with helping me with the microstructural characterization of the specimens. Without his help, I would not have been able to finish my project and I am grateful for his help.

I thank Robert (Ben) Lee and Allyson Barrett of the Department of Dental Biomaterials for their assistance in the mechanical testing of my specimens in the dissertation project. I thank Dr. Anusavice of the Department of Dental Biomaterials for allowing me to use the resources of his department.

I want to thank Andrew Gerger and Brad Willenberg, respectively, of the MAIC staff for helping with the use of the atomic force microscope that I used for a majority of my research and for helping me attain the scanning electron microscope micrographs used in this dissertation. I want to thank Dr. Stephen Freiman with his help in understanding the work of fracture aspects of my work.

I thank the South East Alliance for Graduate Education and the Professoriate, the Alfred P. Sloan Foundation, the National Consortium for Graduate Degrees for Minorities in Engineering

and Science, and the National Science Foundation for their support in funding my graduate study.

I thank my friends and colleagues, especially Dr. Vasana Maneeratana, Ricardo Torres, and Alma Stephanie Tapia for their help, advice, and support during my time at the University of Florida. Finally, I thank my mother and father for all the help and support they have given me that has allowed me to accomplish my goal of receiving my Ph.D.

# TABLE OF CONTENTS

	<u>page</u>
ACKNOWLEDGMENTS .....	4
LIST OF TABLES .....	8
LIST OF FIGURES .....	9
ABSTRACT .....	11
CHAPTER	
1 INTRODUCTION .....	13
Introduction.....	13
Goals .....	13
Objectives .....	14
Structure of Dissertation .....	15
2 LITERATURE REVIEW .....	16
Bilayer Composites.....	16
Glass Ceramics .....	17
Diffusion Bonding.....	19
Work of Fracture.....	20
Fractal Geometry .....	21
3 MATERIALS AND METHODS .....	27
Sample Preparation.....	27
Preparation of Glass-Ceramic Core.....	27
Preparation of Glass Veneer.....	28
Preparation of Bilayers.....	29
Microstructural Analysis .....	29
Phase Identification .....	29
Aspect Ratio .....	29
Fracture Strength .....	30
Fracture Toughness.....	32
Strength Indentation .....	32
Fractography.....	32
Work of Fracture.....	33
Fractal Dimension.....	35
Statistical Analysis.....	37
4 RESULTS AND DISSCUSION.....	41

Microstructural Analysis .....	41
Phase Identification .....	41
Aspect Ratio .....	42
Fracture Strength .....	43
Fracture Toughness.....	44
Work of Fracture.....	45
Soda-Lime-Silica Glass.....	45
Dental Materials .....	48
Fractal Dimension.....	50
Soda-Lime-Silica Glass.....	50
Baria Silica Glass .....	52
Dental Materials .....	53
5 CONCLUSIONS .....	79
APPENDIX DETERMINATION OF THE HURST EXPONENT FOR SILICA GLASS.....	81
Background on the Hurst Exponent.....	81
Measurement Methods for Determining Hurst Exponent .....	82
Hurst Exponent for Silica Glass .....	84
BIOGRAPHICAL SKETCH .....	92

## LIST OF TABLES

<u>Table</u>	<u>page</u>
3-1 Chemical composition of IPS e.max® Press .....	39
3-2 Chemical composition of IPS e.max® Ceram .....	39
3-3 AFM scan areas used to determine optimum scan areas for fractal dimension measurements of fracture surface of baria silica glass.....	40
4-1 Fracture strength, fracture toughness determined from strength indentation (SI), and fracture toughness determined from fractography (F) for e.max® Ceram (EV), e.max® Press (EC), bilayer with crack initiation in veneer (BV), and bilayer with a flaw produced in the core (BC).....	57
4-2 Work of fracture values calculated for chevron notch specimens using cross-sectional area (ACS) and actual fracture surface area based on probe tip radius, equilibrium bond length, and free volume $a_0$ . .....	57
4-3 Comparison of work of fracture and fracture toughness, based on work of fracture, for unstable crack growth soda-lime-silica glass specimens .....	57
4-4 Work of fracture $\gamma_{WOF}$ , based on cross-sectional area ( $A_{CS}$ ) and fracture surface area ( $A_F$ ) for veneer, core, and bilayer bars.....	57
4-5 Fractal dimensional increment for soda-lime-silica glass fracture surface regions measured using atomic force microscopy and the Gwyddion and WSxM software .....	58
4-6 Fractal dimensional increment for e.max® Ceram (EV) and the e.max® Press (EC) ceramics measured using AFM and Gwyddion software .....	58
4-7 Fractal dimensional increment for bilayer specimens using AFM and Gwyddion .....	58
A-1 Hurst exponent for mirror region of silicate glasses from different experimental methods.....	87

## LIST OF FIGURES

<u>Figure</u>	<u>page</u>
2-1 Diffusion bonding process.....	24
2-2 Replication technique for creation of samples for slit island method.....	25
2-3 Production of island from polishing .....	25
2-4 Profile technique using fracture surface replica.....	26
3-1 Cross-section of bilayer specimens.....	38
3-2 Diagram of distances used for computation of centroid for bilayer specimens.....	38
3-3 Diagram of distances used for computation of moment of inertia.....	39
4-1 X-ray diffraction pattern for e.max® Press (EC) core ceramic showing that lithium disilicate are the crystals present in the glass-ceramic.....	59
4-2 X-ray diffraction pattern of e.max® Ceram (EV) veneer ceramic showing veneer material has a amorphous pattern .....	60
4-3 SEM micrographs of polished and etched surface of e.max Ceram (EV) veneer ceramic .....	61
4-4 SEM image of polished and etched surface of e.max Ceram (EC) core ceramic showing the presence of needle-like nanofluorapatite crystals.....	62
4-5 Energy dispersive X-ray spectroscopy (EDS) of e.max® Ceram (EV) veneer ceramic.....	63
4-6 SEM micrograph of polished and etched surface e.max® Press (EC) core ceramic at a magnification of 10000x.....	63
4-7 SEM micrograph of polished and etched surface e.max® Press (EC) core ceramic at a magnification of 5000x .....	64
4-8 SEM micrograph of polished and etched surface e.max® Press (EC) core ceramic at a magnification of 10000x .....	66
4-9 SEM image of fracture surface of chevron-notched soda-lime-silica flexure specimen showing that fracture surface is all mirror and no mist or hackle is present .....	67
4-10 AFM scan image of soda-lime silica glass fracture surface at a scan area of (750 nm) <sup>2</sup> .....	68

4-11	Fracture surface area ( $A_F$ ) as a function of scan area side length ( $\eta$ ) for chevron-notched soda-lime-silica bars.....	69
4-13	Fracture surface area ( $A_F$ ) as a function of scan area side length ( $\eta$ ). .....	71
4-14	Fracture surface area ( $A_F$ ) and adjusted fracture surface area (Adj. $A_F$ ) as a function of scan area side length ( $\eta$ ) for e.max® Ceram (EV) veneer bars.....	72
4-15	Fracture surface area ( $A_F$ ) as a function of scan area side length ( $\eta$ ) for e.max® Press (EC) core bars .....	73
4-16	Fracture surface area ( $A_F$ ) as a function of scan area side length ( $\eta$ ) for veneer-indent (BV) and core-indented (BC) bilayers.....	74
4-17	Fractal dimension increment ( $D^*$ ) of baria silica glass, plotted against scan area, determined from Gwyddion for mirror, mist, and hackle region.....	75
4-18	AFM scan image of e.max® Ceram (EV) veneer ceramic and e.max® Press (EC) core ceramic fracture surface at a scan area of $(750 \text{ nm})^2$ . .....	76
4-19	SEM images of veneer-indented bilayer (BV) fracture surface.....	77
4.20	SEM images of core-indented bilayer (BC) fracture surface.....	78

Abstract of Dissertation Presented to the Graduate School  
of the University of Florida in Partial Fulfillment of the  
Requirements for the Degree of Doctor of Philosophy

DETERMINING THE ROLE OF FRACTAL GEOMETRY AND FRACTURE ENERGY IN  
BRITTLE BILAYER MATERIALS

By

Robert Lee Smith

August 2009

Chair: John J. Mecholsky Jr.

Major: Materials Science and Engineering

Many applications in the ceramic field require bilayer design to be successful. One example is the application of bilayers in dentistry for all ceramic crowns and bridges. Although fracture in bilayers has been studied, research has not explored if the fracture surface changes as a crack travels from one material to another in a bilayer and if a change in the fracture surface reflects changes in the mechanical properties of the bilayer. The work of fracture, fractal dimension, fracture strength, and apparent fracture toughness were determined for two sets of bilayer bars composed of e.max Ceram® veneer bonded to e.max Press® core. The work of fracture was determined from the actual fracture surface area, using atomic force microscopy, to determine if the work of fracture can be used to estimate the minimum fracture energy of the materials. The location of crack initiation was examined to see if the work of fracture is the same in both sets of bilayers and if the fracture process results in the veneer and core having the same fractal dimension.

It was confirmed that the location of crack initiation did change the work of fracture of the bilayers but did not change the fractal dimension of the two materials in the bilayer. The work of fracture was used to estimate the minimum fracture energy of the ceramic monoliths and bilayers. Using the actual fracture surface to determine the work of fracture resulted in a

decrease in the work of fracture but did not estimate the theoretical minimum fracture energy of the dental materials. The work of fracture for the bilayer was dependent on the material that the crack initiated in, further indicating that the selection of the materials used in these bilayers is important in designing these bilayer structures. The fractal dimensions of the veneer and core in the bilayers were similar to that of the monolithic specimens. This implies that the fracture process does not change the fractal dimension of these materials and that the fractal dimension is an intrinsic property of these ceramics.

## CHAPTER 1 INTRODUCTION

### **Introduction**

The critical element that controls the fracture process has not been fully determined for bilayer composite materials such as dental prosthetics or ceramic armor. Selection of the proper material is critical to performance if the material in which fracture initiates controls the fracture properties of the entire composite. There are several properties that are important in determining the effect of the location of crack initiation on the fracture process of a material: fracture toughness, fractal dimension, and work of fracture. Fracture toughness is the resistance to crack propagation in a material. The fractal dimension is a quantitative measure of the tortuosity of a surface at multiple length scales. The work of fracture is defined as the total energy consumed to produce a unit area of fracture surface during the fracture process. These properties can be used together in multilayer composites to study the effect of the initiation of fracture on the fracture process in bilayers.

### **Goals**

The goal of the proposed research is to determine if the fracture surface area and the fractal dimension of materials in a bilayer change as a crack travels from one material into another and if a change in the fracture surfaces determines the mechanical properties of the bilayer structure. This goal will be accomplished by testing the fracture toughness, work of fracture, and fractal dimension of a glassy veneer bonded to a glass-ceramic dental core. Knowledge of the energy contributed to create the fracture surface in ceramics will help engineers better understand the total energy to generate fracture. This will help to better design brittle materials and bilayer structures that are used in several disciplines like dentistry and armor protection, where fracture resistance and materials selection is critical. Knowledge of changes in the fractal dimension of

fracture surfaces for bonded ceramic materials will give a better understanding of the role that the fracture process has in determining the fractal dimension of the materials. This will aid in the further use of the fractal dimension as a tool in characterizing the fracture of ceramic materials.

### **Objectives**

To accomplish the goal of this research, the following hypotheses are proposed:

1. Test the hypothesis that the work of fracture based on the actual fracture surface area can be used to estimate the fracture energy of ceramic materials.
2. Test the hypothesis that the work of fracture of a ceramic bilayer will be the same regardless of the location of crack initiation.
3. Test the hypothesis that the fractal dimension of the two materials in a bilayer will be the same regardless of the location of crack initiation.

A veneer and a core dental ceramic were chosen as the materials used to test the stated hypotheses. The veneer chosen was IPS e.max® Ceram, a fluorapatite glass-ceramic, and IPS e.max Press®, a lithium disilicate glass-ceramic. These materials were chosen because bilayers of the materials are used in dentistry, so the mechanical properties (elastic modulus, fracture strength, fracture toughness, etc.) of the materials have been studied [1-5]. This allows for comparison of the mechanical properties studied in this dissertation to what other researchers have measured. The mechanical properties of the two materials are different enough in order to determine if location of crack initiation changes the mechanical properties of these materials. The veneer and core have been shown to bond well [3, 4, 6], producing a strong bond at the interface between the two materials. This means a crack that propagates in one layer should continue to propagate into the second layer without delaminating at the interface.

A series of experiments have been determined to test the hypotheses for this project:

1. The microstructure was analyzed and the fracture strength and apparent fracture toughness were determined for the veneer, the core and for two sets of bilayers.
2. The work of fracture, using the cross-sectional area and the fracture surface area, was determined for a control group of soda-lime-silica (SLS) glass under stable and unstable crack growth.
3. The work of fracture, using the cross-sectional area and the fracture surface area, was determined for the veneer, the core, and for the two sets of bilayers
4. The fractal dimension was measured for a control group of SLS glass and baria silica glass.
5. The fractal dimension was measured for the veneer, the core, and two set of bilayers.

### **Structure of Dissertation**

Chapter 2 is a compilation of selected literature explaining the concepts of the work of fracture and fractal dimension, and defining bilayer materials, glass-ceramics, and diffusion bonding. Chapter 3 describes the materials selected for the study and the process used to prepare these materials. The experimental procedures used to answer the hypotheses discussed in the objectives are also explained in this chapter. Chapter 4 details the results from the experiments described in Chapter 3 and interprets the meaning of the results. Chapter 5 summarizes the dissertation and discusses whether the hypotheses were answered from the experiments. The dissertation concludes by addressing the concept of the Hurst exponent and its relationship to the fractal dimension for soda-lime-silica glass in the Appendix.

## CHAPTER 2 LITERATURE REVIEW

In this chapter, bilayer composites, diffusion bonding, and glass-ceramics are discussed to give background on the dental materials and fabrication methods used in the dissertation. The two parameters discussed in the objective, the work of fracture and the fractal dimension, are defined and background is given on the previous methods used to determine these properties.

### **Bilayer Composites**

A bilayer material is a composite material in which two different materials are bonded together. Bilayer materials are joined by either bonding the two materials together using a welding or diffusion bonding technique or by using an interlayer like an adhesive to bond the two materials together. As in all composites, bilayer materials are designed to combine the advantages of both materials to produce an optimum structure. Bilayers are used in a variety of applications from protective coatings on metal substrates that are used in the aerospace industry to titanium alloys bonded with a bioactive glass coating for bone implants [7].

Ceramic bilayers that are used to produce dental prostheses have had an increase in use over the years. The use of a bilayer composite allows for the aesthetic and mechanical properties needed for dental prostheses. All-ceramic dental bilayers for prostheses are made of two materials: a glass veneer that is matched to the appearance of the surrounding teeth and the glass-ceramic core that provides the stiffness and fracture resistance that is needed for dental prostheses. The veneer must also be matched in thermal expansion and contraction coefficient to minimize the risk for transient crack formation and residue tensile stress.

The mechanical properties of these bilayer materials are dependent on the mechanical properties of the two materials and the interface between these materials. If a crack initiates and propagates from the tensile surface of one the less tough layer, e.g., the veneer layer in a veneer-

core all-ceramic dental restoration, the propagation of the crack is dependent on the fracture toughness of the interface and the second material [5, 8]. If the fracture toughness of the interface is greater than the fracture toughness of the two materials in the bilayer, the crack will continue to propagate into the second material. However, if the interface is less resistant to fracture than the second material, then the crack will propagate along the interface of the two materials and perhaps nullify the benefits of using a more fracture resistant material in the bilayer. Taskonak et al. [9] showed that for lithia-disilicate based fixed partial dentures, cracks that initiated in the veneer propagated across the interface and into the core. Even though the core had a greater fracture toughness than the veneer, the crack was not impeded by the core at the interface. This implies that the interface is tougher than the core. For yttria-stabilized tetragonal zirconia polycrystals fixed partial dentures, cracks that initiated in the veneer propagated through the veneer and stopped at the interface of the two materials. Delamination occurred at the interface before a secondary crack initiated in the core. This implies that the core was tougher than the interface and that delamination controlled the fracture process of the bilayer.

Although the mechanical properties of ceramic bilayers and multilayers have been explored [4, 5, 10-15], research has not explored if the fracture surface changes as a crack travels from one material to another in a bilayer and if a change in the fracture surface determines the mechanical properties of the bilayer structure. Analysis of the work of fracture and the fractal dimension will result in a better understanding of fracture surface of each material in the bilayer affects the mechanical properties of the composite and if the location of crack initiation changes the fracture surface and mechanical properties of the bilayer structure.

### **Glass Ceramics**

Glass-ceramics are polycrystalline ceramic materials formed from a base glass through the controlled nucleation and crystallization of crystals from the glass [16]. The crystals are

contained in a matrix of the base glass. Glass-ceramics are different from traditional ceramics where the crystalline material is introduced when the ceramic composition is prepared. It has been known for a long time that glasses can be crystallized to form polycrystalline ceramics. Réaumur, a French chemist, produced polycrystalline material from glass by heating glass bottles, packed in sand and gypsum, to a high temperature for several days [17]. Réaumur experiments resulted in the creation of opaque, porcelain-like objects that had low mechanical strength and a distorted shape compared to the original shape of the bottles. This was due to the inability to control the crystallization process.

The invention of true glass-ceramics did not occur until the mid-1950s [16]. S. D. Stookey, a glass chemist and inventor at Corning Glass Works, was planning to precipitate silver particles in lithia silicate ( $\text{Li}_2\text{O-SiO}_2$ ) to create a permanent photographic image. He accidentally overheated the glass overnight, producing a white ceramic with no net change in shape and an unusual strength for a glass. Upon further analysis, Stookey determined that lithium disilicate ( $\text{Li}_2\text{Si}_2\text{O}_5$ ) crystals, nucleating from the silver particles, had been created in the glass. Stookey's experiment produced a new type of material had been discovered that had applications in several fields.

Glass-ceramics have advantages over glass when it comes to mechanical properties and advantages over metals and organic polymers in the areas of thermal, chemical, biological, and dielectric properties. The presence of grain boundaries and cleavage planes impede fracture propagation while the crystals cause crack deflection, resulting in a greater fracture toughness compared to glass [16]. Glass-ceramics exhibit little to no expansion on heating and have a high temperature stability. This allows glass-ceramic to be used in high temperature application, where metals cannot be used, e.g., cookware. The high chemical durability and translucency or

opacity of glass-ceramics makes glass-ceramic a useful material in places where the corrosion of metal is a problem. Another advantage of glass-ceramics is that a glass-working process can be used to create objects resulting in the use of high-speed automatic machining and a faster processing time when compared with the techniques used in conventional methods.

The most important features of glass-ceramics are that they are applicable over a wide range of compositions and variations can be controlled through the heat treatment process [17]. Various crystal types can be developed in controlled proportions resulting in the ability to vary the physical characteristics of glass-ceramics in a controlled manner. This feature allows glass-ceramics to be designed and created for a multitude of applications.

### **Diffusion Bonding**

Diffusion bonding involves the interdiffusion of atoms across the interface of two materials, held in contact with each other, resulting in the bonding of the two materials [18]. The bonding of these materials involves holding a pre-machined component under pressure at an elevated temperature in a protective environment. The pressure applied to the joining materials must cause the edges to move within range of the atomic forces but below a pressure that would cause macrodeformation in either material (Figure 2-1). The temperature range for diffusion bonding is between 0.5 and 0.8 of the lower melting temperature of either of the two materials [19]. Diffusion bonding usually requires a minimum of 60 minutes to successfully bond the materials. The main advantages of diffusion bonding are 1) the material at the joint has the same strength and plasticity as the bulk of the parent materials, 2) the bonding temperature is not as high as other joining processes, and 3) more types of joints can be formed compared with other joining processes [18].

Although diffusion bonding is used mostly to bond metals to metals or metals to non-metals, it has been used to bond ceramics to ceramics [20]. Ceramic to ceramic bonding is

mainly carried out in the solid phase with heat being applied by radiant, induction, direct or indirect resistance heating. Some ceramics do not incur the problem of oxidation hindering bonding since the ceramics themselves are oxides. The bonding of some ceramics, like the bonding of a glass-ceramic to a glass, has a similar advantage of bonding similar metal alloys: the ability to increase the mechanical properties of an object but keeping the favorable properties of the weaker material. This is observed in dental ceramics, where a transparent or translucent veneer is diffusion bonded to a stronger and more fracture resistant glass-ceramic core. This makes the dental ceramic stronger than the veneer and allows it to maintain its aesthetic properties.

### **Work of Fracture**

The fracture energy ( $\gamma$ ) of a material is defined as the energy per unit area required to fracture an infinite body into two separate halves [21]. Defined in another way,  $\gamma$  is the energy required to break the bond between two atoms per unit area. When a specimen is tested in a manner that allows for the stable growth of a crack, the average fracture energy can be determined for the specimen. This average fracture energy is called the work of fracture ( $\gamma_{WOF}$ ). The work of fracture is defined as the total energy consumed to produce a unit area of fracture surface during the fracture process [21] and is calculated from the equation:

$$\gamma_{WOF} = \frac{W}{A_{CS}} \quad (2-1)$$

where  $W$  is the work and is equal to the area under the load-displacement curve and  $A_{CS}$  is the cross-sectional area of the fracture surface. In theory, if it is assumed that all of the work from loading is dissipated by the breaking of the bonds, then the average  $\gamma = \gamma_{WOF}$  [29].

The work of fracture has been used as a method to determine the fracture toughness ( $K_{IC}$ ) of materials [22-24] based on Irwin's equations:

$$K_C = \sqrt{2E'\gamma} \quad (2-2)$$

where  $E'$  is the elastic modulus ( $E$ ) for plane stress or  $E/(1-\nu^2)$  [ $\nu$  is Poisson's ratio] for plain strain and  $\gamma = \gamma_{\text{WOF}}$ . The work of fracture has also been used as a separate parameter to describe the fracture properties of various materials, including biological [25-28], ceramics [23, 29-34], polymer [35, 36], and metal materials [22, 37]. The advantages of using the work of fracture are that it does not require knowledge of the stress intensity, the geometry of the notch, the notch tip acuity, or the linearity of the material.

In most cases,  $K_C$  values calculated using  $\gamma_{\text{WOF}}$  have led to an overestimation of  $K_C$  when compared with values calculated from methods that are more conventional [22, 23]. This is due to the assumption that  $\gamma = \gamma_{\text{WOF}}$  based on the equation used to calculate  $\gamma_{\text{WOF}}$  (Equation 2-1). This assumption is based on the idea that all of the energy of the fracture process results in the creation of two atomically smooth surfaces, resulting in the cross-sectional area being used as the actual fracture area being created by the fracture process [29]. However, it is apparent that fracture surfaces are not absolutely smooth, even in the fracture mirror region [38]. Since the energy used to fracture materials results in the creation of a rough and tortuous fracture surface, then using the actual fracture surface area of the material, which is greater than the cross-sectional area, to calculate  $\gamma_{\text{WOF}}$  would result in a better approximation of the theoretical fracture energy of the material.

### **Fractal Geometry**

Fractal geometry, a non-Euclidean geometry, can be used to quantitatively describe irregular shapes and surfaces [39], e.g., a maple leaf or a head of cauliflower. Fractal objects are defined as objects that are self-similar, scale invariant, and exhibit fractional dimensions. A self-

similar object is an object that has multiple parts that are similar to the entire object. A scale invariant object is an object that looks the same at different magnification scales.

From Mandelbrot's early work in fractal geometry, especially in evaluating the fracture surface of steels [40], fractal geometry has been shown to be a useful tool in the fields of science and engineering. The basic quantitative component of fractal geometry is the fractal dimension (D). The fractal dimension is a non-integer number with a Euclidean and non-Euclidean component. The Euclidean component describes the topological dimension of the object, e.g., 1 for a line and 2 for a square or circle. The non-Euclidean component, called the fractal dimensional increment ( $D^*$ ), describes the level of irregularity of the object from its Euclidean geometry. The fractal dimensional increment ranges from 0 to 1, with the level of irregularity increasing as the increment increases. For example, broccoli has a fractal dimension of 2.66 [41], where 2 denotes that it is a surface and 0.66 denotes the fractal component and the level of irregularity in the surface of broccoli.

In materials science, fractal geometry has been used as an analytical tool to quantify the fracture surfaces of brittle and ductile materials [42-48]. Fracture surfaces have a fractal dimension of  $2.D^*$  with a fractal dimension of 2.1 denoting a fracture surface that is relatively flat and a fractal dimension of 2.9 denoting a fracture surface that is volume filling.

Several methods have been used to measure the fractal dimension of a fracture surface. The measurement of the contours of the fracture surface is one of the most frequently used methods. There are two main boundary contour methods: the slit-island method [40], which examines the contour parallel to the plane of the fracture surface, and the profile method, which examines the contour perpendicular to the plane of the fracture surface [39].

The slit island technique uses the fracture surface to determine the fractal dimension. The fracture surface of a specimen, or a replica of the fracture surface, is plated in a visible coating such as a gold-palladium sputter coating to make the surface more visible (Figure 2-2). The specimen is mounted in epoxy or another mountable material and polished parallel to the fracture surface until parts of the fracture surface, called islands, are visible (Figure 2-3). From the coastlines of the islands, the fractal dimension is measured using one of two methods: measurement of the perimeter and area of the islands or measuring the length of the “coastline” of the islands (the Richardson method) [49]. A straight line drawn through the data points of a log-log graph of the area versus the perimeter results in a line that has a slope equal to  $-D^*(1-D)$ . For the Richardson method, the perimeter is measured at different length scales using the following equation:

$$L(\eta) = L_0 \eta^{(1-D)} \quad (2-3)$$

where  $L(\eta)$  is the measured perimeter length as a function of the step size,  $L_0$  is the projected perimeter, and  $\eta$  is the step size.  $D^*$  can be determined from the log-log plot of the perimeter versus the step size.

The profile method measures the profile of the fracture surface (Figure 2-4). The profiles are obtained using microscopy, e.g., optical, secondary electron, and scanning tunneling. From these profiles, the fractal dimension can be determined using Equation 2-3 where  $L_0$  is the projected length of the profile and  $L(\eta)$  is the measured length of the profile.

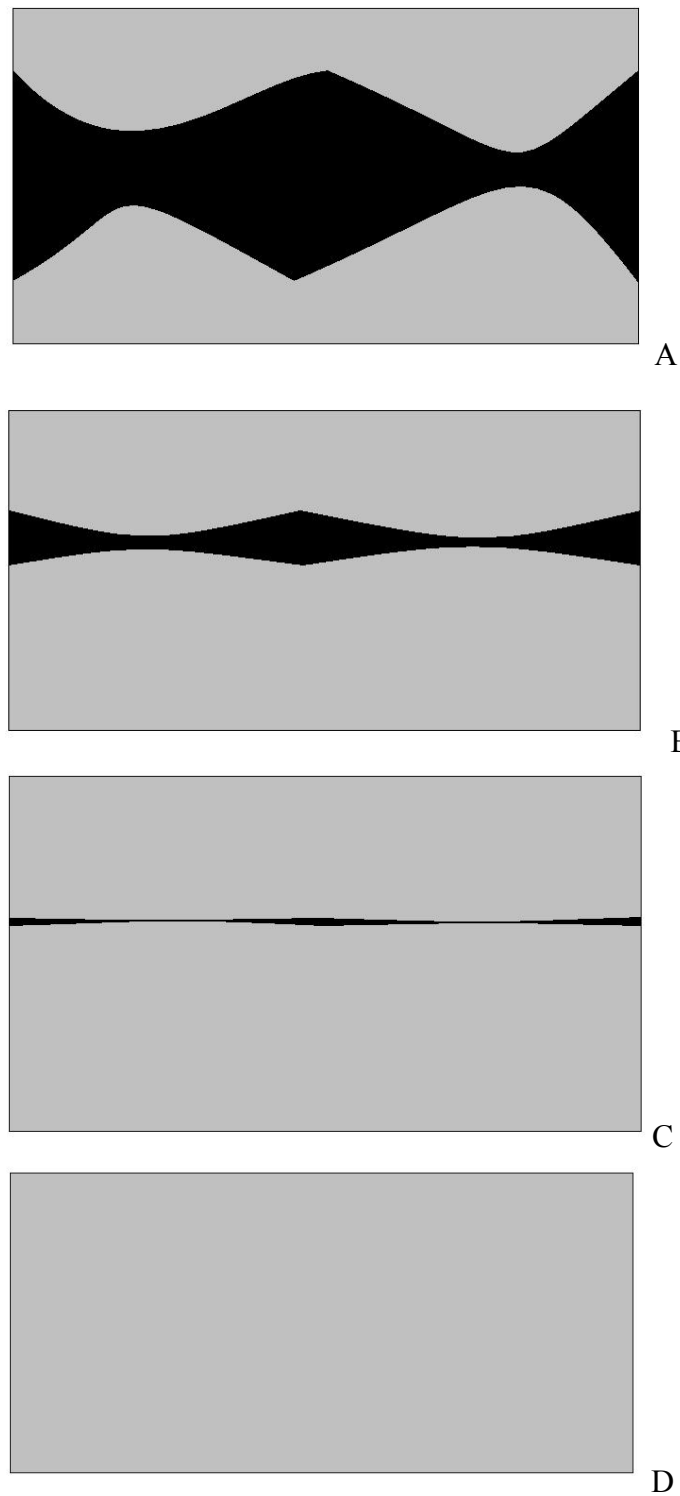


Figure 2-1. Diffusion bonding process. A) Initial contact. B) Plastic deformation. C) Diffusion processes fill microvoids. D) Bonding completed. [Adapted from Lancaster, J. F. (1999) Metallurgy of Welding, 6<sup>th</sup> edn. Woodhead Publishing, Cambridge, UK].

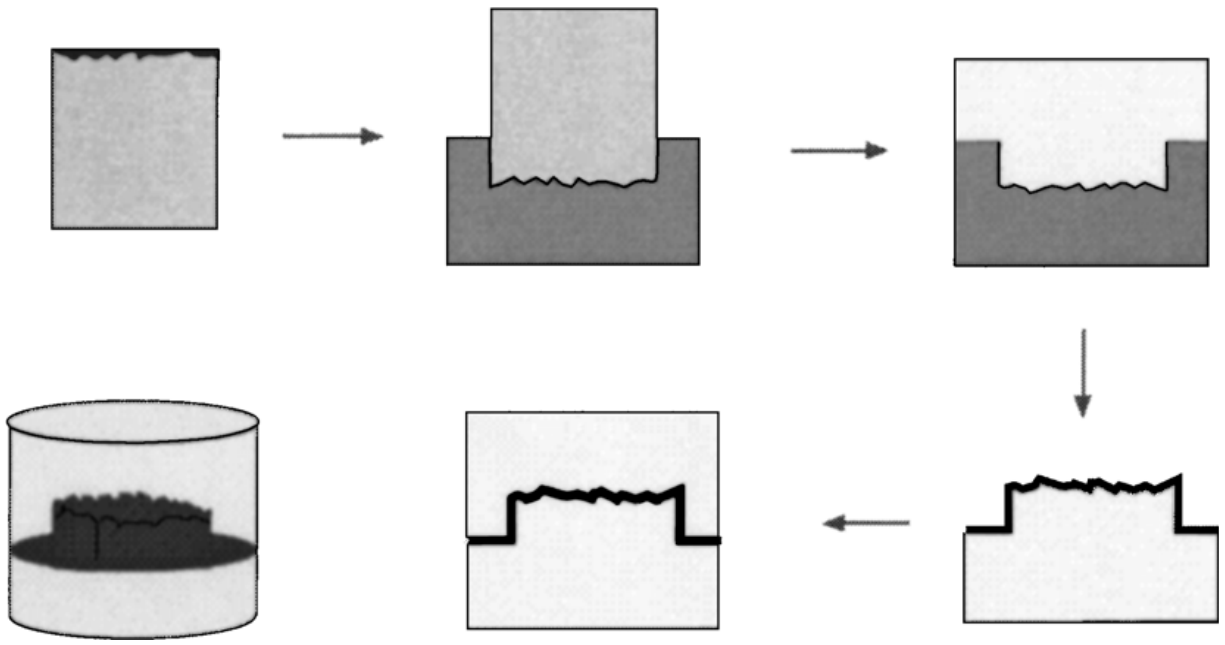


Figure 2-2. Replication technique for creation of samples for slit island method. [Source: Hill, TJ, Della Bona, A, Mecholsky, JJ (2001) J Mater Sci 36:2651]

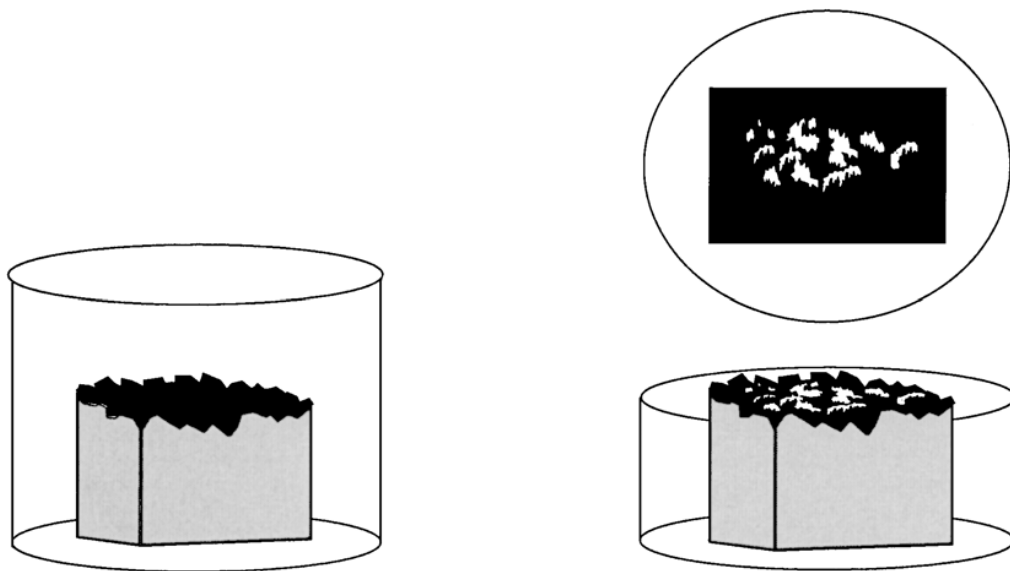


Figure 2-3. Production of island from polishing. [Source: Hill, TJ, Della Bona, A, Mecholsky, JJ (2001) J Mater Sci 36:2651]

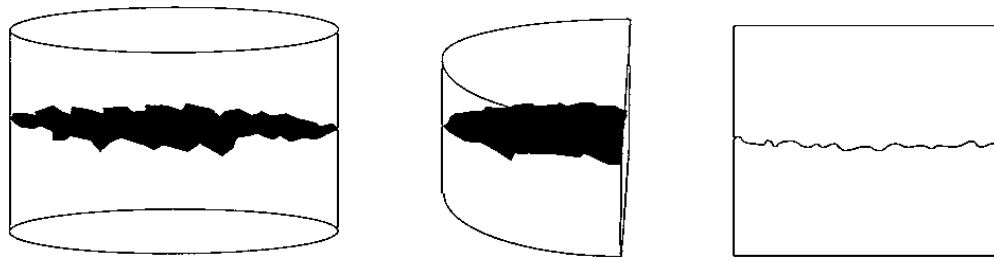


Figure 2-4. Profile technique using fracture surface replica. [Source: Hill, TJ, Della Bona, A, Mecholsky, JJ (2001) J Mater Sci 36:2651]

## CHAPTER 3 MATERIALS AND METHODS

In this chapter, the preparation of the materials used is described for this study. The mechanical and microstructural procedures used to characterize the materials are discussed and the measurement of work of fracture and fractal dimension methods for the dental materials is described.

### **Sample Preparation**

#### **Preparation of Glass-Ceramic Core**

The lithium disilicate dental glass-ceramic cores were prepared using a lost-wax method [4]. A self-curing acrylic resin (Pattern Resin, GC Corp, Tokyo, Japan) was used to prepare the master molds for the IPS e.max Press® (EC) glass-ceramic (Ivoclar AG, Schaan, Liechtenstein). The EC is a lithium disilicate glass-ceramic (Table 3-1). Impressions were made from the master mold using a vinyl polysiloxane impression material (Extrude, Kerr Corp., Romulus, MI). The acrylic resin was poured into the molds and cured to make rectangular bars (25 mm x 4.6 mm x 2.0 mm) using a mill (PGF 100, Cendres & Metaux Sa., Biel-Bienne, Switzerland).

Following the preparation of the resin beams, four specimens were sprued and invested. The resin beams were placed in a preheating furnace (Radiance, Jelrus Int., Hicksville, NY) and a two-stage burnout process was used to remove the resin: 1) the furnace is heated up to 250°C at 5°C/min. and held for 30 min. and 2) the furnace was heated up to 850°C at 5°C/min. and held for 1 hr. After burnout, the EC ingot was placed in an investment cylinder and it was transferred to an isostatic pressing furnace (EP500, Ivoclar AG, Schaan, Liechtenstein). The EC was pressed at a pressure of 5 bar (0.5 MPa) and a temperature of 920°C for 25 min. After pressing, the investment cylinders were removed and cooled for 2 hr. in air. The cooled specimens were divested (removal of investment material) by grit blasting with 80 µm glass beads (Williams

Glass Beads, Ivoclar North America, Amherst, NY) at an air pressure of 0.25 MPa. The sprues were cut away using a diamond disc and excess sprue segments were ground from 120 to 1200 grit using silicon carbide (SiC) paper and polished from 8 to 1 micron using diamond paste (Buehler, Lake Bluff, IL) on polishing cloth (Ultrapol™, Buehler, Lake Bluff, IL) and 1 micron alumina (Micropolish® II, Buehler, Lake Bluff, IL) on polishing cloth (Microcloth®, Buehler, Lake Bluff, IL). All polishing and grinding were performed on a metallographic polishing wheel (Model 41-1512, Buehler, Lake Bluff, IL).

After polishing, the reaction layer from investing was removed by placing the bars in a plastic bottle containing 20 mL of a 1% hydrofluoric solution (Invex Liquid, Ivoclar AG, Schaan, Liechtenstein) and ultrasonically cleaned for 10-30 min. After cleaning, the bars were cleaned again using tap water for 10 s and blown dry using compressed air. After drying, the bars were grit-blasted with 100 µm Al<sub>2</sub>O<sub>3</sub> particles (Blasting Compound, Williams-Ivoclar North America Inc., Amherst, NY) at an air pressure of 0.1 MPa. Then, the bars were cleaned using a pressurized steam spray.

### **Preparation of Glass Veneer**

The glassy veneer, IPS e.max® Ceram (EV), is described as a fluorapatite glass-ceramic (Table 3-2). Glass veneers were prepared using a sintering process. A veneer powder was mixed with a liquid (Ivoclar AG, Schaan, Liechtenstein) to obtain a slurry solution. This solution was then poured into a silicone mold, condensed by vibration, dried, and sintered in a furnace (P80, Ivoclar AG, Schaan, Liechtenstein) by heating to 800°C at 60°C/min., held for 2 min., and cooled to 180°C. A vacuum was applied between 450°C to 759°C. Following the sintering process, any excess veneer was ground of with a 75 grit circular diamond disk and polished down to a 1 µm finish using a metallographic polishing wheel. All veneer bars have the same dimensions (25 mm x 4.6 mm x 2.0 mm) as the core ceramic.

## **Preparation of Bilayers**

The veneer and core ceramics were bonded together using a sintering process. The prepared EC bars were veneered with the EV. The veneer powders were mixed with a liquid (Ivoclar AG, Schaan, Liechtenstein) to obtain a slurry solution. This solution was brushed onto the EC. The bilayers were then sintered in a furnace (P80, Ivoclar AG, Schaan, Liechtenstein) by heating to 800°C at 60°C/min., held for 2 min., and cooled to 180°C. A vacuum was applied between 450°C to 759°C. Three layers of veneer were sintered on each EC bar. Following the sintering process, any excess veneer was ground off with a 75 grit circular diamond disk and polished down to a 1 µm finish using a metallographic polishing wheel. The dimensions of the bilayers were set to be similar to the monolithic veneer and core (25 mm x 4.6 mm x 2.1 mm) with the veneer having a thickness of 1.1 mm and the core having a thickness of 1.0 mm.

## **Microstructural Analysis**

### **Phase Identification**

X-ray diffraction (XRD) was performed on the EC and EV to determine if both materials were glass-ceramics. Using a mortar and pestle, a sample of the glass ceramic was ground into a fine powder. The powder was placed on a glass slide using double-sided tape. The specimen was scanned at a rate of 3°/min. over a 2θ range of 10-60°.

### **Aspect Ratio**

The aspect ratio of the crystals in the EC glass ceramic specimens was determined using a scanning electron microscope (SEM). Samples of the glass ceramic were mounted in epoxy and polished down to a 0.05 µm finish. After polishing, the specimens were etched in 2.5 % hydrofluoric (HF) for 10 s, cleaned in tap water, ultrasonically cleaned for 5 min. in isopropanol, and air-dried using compressed air. The top and sides of the epoxy mount was painted with carbon paint before sputter coating with carbon. Three micrographs each were taken from two

specimens. The major and minor axes of five crystals from each micrograph were measured to calculate the aspect ratio of the glass-ceramics.

### **Fracture Strength**

As a control group, the strength of the glass veneer and core glass-ceramic were measured. Five bars of EC and EV each were prepared for testing. The fracture strengths of the bilayer bars was tested using the strength indentation technique [50]. A Vickers indent was placed in the center of the tensile surface of the bars using a microhardness machine (Model, Buehler, Lake Bluff, IL) with an indent load of 1 kgf for EV and 2 kgf for EC. After indentation, the bars were tested in four-point flexure using a universal testing machine (Model 4465, Instron Corp, Norwood, MA) at a crosshead speed of 0.2 mm/min. with a support span of 20 mm and a load span one-third of the support span. The flexure strength of the bars was calculated using the equation:

$$\sigma_F = \frac{FL}{bd^2} \quad (3-1)$$

where  $\sigma_F$  is the flexural strength of the specimen, F is the load at failure, L is the support span, b is the specimen width, and d is the specimen thickness.

For the bilayer bars, two sets of five specimens were fabricated for flexure testing. The first set was indented on the tensile surface of the EV layer of the bilayer with an indent load of 1 kgf. The second set was indented on the tensile surface of the EC layer of the bilayer with an indent load of 2 kgf. Because of the difference in the elastic moduli of the two layers, composite beam theory was used to calculate the fracture strength of the bilayers. We followed the method outline in Beer and Johnston [51] and applied by Thompson [5] to dental ceramics. The composite beam was transformed into a uniform beam of EC. This was done by calculating the

transformation factor ( $n$ ), the centroid ( $y$ ), and the moment of inertia ( $I$ ) for the transformed beam.

The transformation factor is the ratio of the elastic modulus of EC [96 GPa] [52] and EV [64 GPa] [52]. This ratio is 3/2, therefore  $n = 1.5$  and the width of EV is transformed from 4.6 mm to 3.1 mm (Fig. 3-1). With this transformation, the centroid can be determined for the composite beam. Using a reference axis set at the tensile surface of the transformed beam (Fig.3-2),  $y$  can be determined using

$$y = \frac{[ABC + DEF]}{[BC + EF]} \quad (3-2)$$

where A, B, C, D, E, and F are the distances for the transformed beam (Fig. 3-2). Once the centroid has been determined, the moment of inertia for the beam can be determined based on the distances in Fig. 3-3 and from the equation

$$I = \left[ \frac{1}{12} ab^3 + ab(c - d)^2 \right] + \left[ \frac{1}{12} ef^3 + ef(g - h)^2 \right] \quad (3-3)$$

With the centroid and moment of inertia known for the composite beam, the flexure stress  $\sigma$  can be determined for the composite beam. The flexure stress is calculated from the equation

$$\sigma = \frac{Mc}{I} \quad (3-4)$$

where  $M$  is the maximum moment and  $c$  is the distance from the bottom of the beam to the centroid. For four-point flexure with a load span 1/3 of the support span,  $M$  is expressed as

$$M = \frac{PL}{6} \quad (3-5)$$

## Fracture Toughness

The fracture toughness of the bilayer and monolithic bars was determined using two methods: 1) the strength indentation technique and 2) fractography.

### Strength Indentation

The strength indentation technique uses an indent, in this case a Vickers indent, to introduce a critical crack in the tensile surface of a flexure bar. The advantage of using this method is that the crack length does not have to be known to calculate the fracture toughness.

The fracture toughness is calculated using the following equation [50]:

$$K_C = 0.59(E/H)^{1/8}(\sigma_F P^{1/3})^{3/4} \quad (3-6)$$

where  $K_C$  is the fracture toughness,  $E$  is the elastic modulus of the specimen,  $H$  is the hardness of the specimen,  $\sigma_F$  is the fracture strength of the specimen, and  $P$  is the indent load. For the bilayer composites,  $E$  was determined from the upper bound of the Rule of Mixtures, i.e.,

$$E_B = E_{EV}A_{EV} + E_{EC}A_{EC} \quad (3-7)$$

where  $E_B$  is the elastic modulus of the composite,  $A_{EV}$  is the area fraction of the veneer in the bilayer,  $E_{EV}$  is the elastic modulus of the core, and  $A_{EC}$  is the area fraction of the core in the bilayer.

### Fractography

The fracture toughness of the bars was calculated using fractography. An optical microscope (Olympus BHMJ, Olympus, Tokyo, Japan) was used to measure the critical flaw size. The fracture toughness was calculated using the equation [53]:

$$K_C = Y\sigma_F\sqrt{c} \quad (3-8)$$

where Y is a geometrical constant for the shape of the crack and loading geometry that has a value of 1.65 for indent-induced surface cracks, with a local residual stress [54], and c is the flaw size. The flaw size was calculated as

$$c = \sqrt{ab} \quad (3-9)$$

where a is the crack depth and b is the half of the crack width.

### Work of Fracture

The work of fracture was measured for soda-lime-silica (SLS) glass as a control group and for the bilayer and monolithic dental ceramic bars. Two equations were used to determine  $\gamma_{WOF}$  associated with the following methods: 1) the cross-sectional area approach (Equation 2-1) and 2) the actual fracture surface area ( $A_F$ ) instead of the cross-sectional area method, i.e.:

$$\gamma_{WOF} = \frac{W}{A_F} \quad (3-10)$$

Since the crosshead displacement of the testing machine does not accurately measure the midpoint deflection ( $\delta$ ) of the flexure specimens,  $\delta$  was calculated using the equation:

$$\delta = \frac{\varepsilon L}{6d} \quad (3-11)$$

where  $\varepsilon$  is the strain to failure and is determined from the equation

$$\varepsilon = \frac{\sigma_F}{E} \quad (3-12)$$

Unstable fracture was accomplished using strength indentation [50] in flexure while stable fracture was accomplished using a chevron-notch (Figure 4-9) in flexure [55]. Three sets of bars were used for the unstable fracture test: 1) 45 mm x 4 mm x 3 mm bars were Vickers indented with a load of 2000 gf load and tested in four-point flexure, 2) 55 mm x 10 mm x 5.7 mm bars were Vickers indented with a load of 1000 gf and tested in three-point flexure, and 3) 55 mm x 10 mm x 5.7 mm bars were Vickers indented with a load of 2000 gf and three-point flexure.

The chevron-notched bars, with dimensions of 45 mm by 4 mm by 3 mm, were fabricated using a low speed diamond saw (South Bay Model 650, South Bay Technology, San Clemente, CA). The notches were cut using a diamond blade with a thickness of 0.15 mm. The specimens were tilted at an angle of 25° using a specially made fixture for the diamond saw.

Both the unstable and stable SLS glass specimens' edges were polished using 240-grit silicon carbide paper to remove or reduce the size of any flaws that were present along the edges. All specimens were tested using a universal testing machine (Model 4465, Instron Corp, Norwood, MA). For the unstable test, the crosshead speed was 0.5 mm/min while the stable tests were conducted at a crosshead rate of 0.03 mm/min.

The fracture surface area was measured using an atomic force microscope (AFM) (Dimension 3100, Veeco Instruments Inc., Woodbury, NY). Using the software that is provided with the AFM (Nanoscope 3D, Veeco Instruments Inc., Santa Barbara, CA), the surface area was determined from the sum of the area of a grid of triangles formed by three adjacent data points in the scans. Eight square scan areas ((750 nm)<sup>2</sup>, (625 nm)<sup>2</sup>, (500 nm)<sup>2</sup>, (375 nm)<sup>2</sup>, (250 nm)<sup>2</sup>, (100 nm)<sup>2</sup>, (50 nm)<sup>2</sup>, and (25 nm)<sup>2</sup>) were used to measure the fracture surface area. Five scans were completed for each scan area per specimen. All scans were conducted in the tapping mode, where the AFM tip is oscillated at the cantilever's resonant frequency causing the tip to intermittently contact the surface. A tapping tip was used to decrease the wear of the AFM tip over time on the hard surface of the materials. Previous AFM work using a contact tip showed a decrease in the surface area measured, over time, due to wear increase the tip radius. All images were scanned at a scan rate of 2-3 Hz and a resolution of 512 pixels per line. All fracture surfaces were cleaned with ethanol to remove the dust and other material from the surface and dried using compressed air.

To determine the fracture surface area, a box counting method was used for which the average surface area of a portion of a selected mirror, mist, and hackle region was measured using the AFM. Then, the surface area value for that representative region was multiplied times the entire cross-sectional area of the region. From the AFM data obtained,  $A_F$  was calculated using the following equation:

$$A_F = \left( A \times \frac{SA}{SS} \right)_{MIRROR} + \left( A \times \frac{SA}{SS} \right)_{MIST} + \left( A \times \frac{SA}{SS} \right)_{HACKLE} \quad (3-13)$$

where  $A$  is the area of a given region (mirror, mist or hackle) of the fracture surface,  $SA$  is the surface area value for that region and  $SS$  is the scan area used to determine  $SA$ . This method was used to calculate  $A_F$  for all of the different scan areas.

### **Fractal Dimension**

The fractal dimensions of SLS glass bars and baria silica glass bars, used as a control group, were determined along with the bilayer and monolithic dental ceramics bars using an AFM. All scans were conducted using a tapping tip at a resolution of 512 pixels per line and a scan rate of 2-3 Hz. All fracture surfaces were wiped clean with ethanol to remove dust and other materials from the surface and dried with compressed air.

To calculate the fractal dimension ( $D$ ) from the AFM data, two software packages were used: 1) Gwyddion and 2) WSxM. Gwyddion is a free and open source software program for scanning probe microscopy data visualization and analysis [56]. Gwyddion uses four methods to calculate the fractal dimension from AFM data: 1) cube counting, 2) triangulation, 3) variance, and 4) power spectrum.

Cube counting uses box counting to determine  $D$  [57, 58]. A grid of cubes with a cube edge length  $m$  is placed over the surface of the AFM image.  $N(m)$  is the number of cubes that

contain at least one pixel. The value of  $m$  is decreased by a factor of two until  $m$  is equal to the distance between two pixels. The slope of the log of  $N(m)$  versus the log of  $(1/m)$  is equal to  $D$ .

For the triangulation method [57], a grid of triangles of side length ( $L$ ) is placed over the image. The areas of all of the triangles is measured and summed to calculate the surface area  $S(L)$  of the image. The grid size is decreased by a factor of 2 until  $L$  is equal to the distance between two pixels. The slope of the log of  $S(L)$  versus the log of  $1/L$  is  $D-2$ .

The variance method is based on the scale dependence of the variance of fractional Brownian motion [59]. An image is divided into cubes and the variance, the power of the RMS value of the heights, is calculated for each cube. The slope of the log-log plot of the variance is equal to  $\beta$  and  $D$  is determined from the equation:

$$D = 3 - \beta/2 \quad (3-14)$$

For the power spectrum method [57, 58], every line profile that makes up the image is Fourier transformed, the power spectrum is analyzed, and power spectra are averaged for all the lines. The slope of the log-log graph of the power spectra is equal to  $\beta$  and  $D$  is determined from the equation:

$$D = 7/2 - \beta/2 \quad (3-15)$$

WSxM is another software program used for data acquisition and processing in scanning probe microscopy [60]. WSxM uses a modified slit-island method, called flooding, to determine the fractal dimension for AFM images. A plane parallel to the fracture surface is used to section the fracture surface image into two halves, producing “islands” of the fracture surface. The log-log graph of the perimeter versus the area for all islands is calculated and the slope of the graph is  $2/D$ . The number of islands measured by WSxM can be changed by increasing or decreasing the size of the islands recognized by the program and the height of the sectioning plane.

To determine the optimal scan areas for determining the fractal dimension, a test was performed measuring the change in fractal dimension as a function of scan area. The mirror, mist, and hackle regions of the fracture surface of baria silica glass bars (30mm x 4mm x 3mm) were Vickers indented at a 500 gf load, fractured in three-point flexure, and scanned at various scan areas (Table 3-3). Baria silica glass was used because it has a similar D value to that of SLS glass [ $D = 0.10 \pm 0.01$ ][61][39]. The values of D were then compared with the fractal dimension of baria silica glass calculated using the slit island method [61]. Using the optimal scan areas, the fractal dimension of the veneer, core, and the two sets of veneer/core bilayer bars was measured and compared.

### **Statistical Analysis**

All statistical analyses were conducted using KaleidaGraph, a graphing and data analysis software package. ANOVA was used to determine if there was a statistical difference or similarity between the means of the variables (aspect ratio, fracture strength, fracture toughness, and fractal dimension) in the experiments. A significance level ( $\alpha$ ) of 0.05 was used in all ANOVA tests. A p-value less than  $\alpha$  ( $p \leq 0.05$ ) denotes a statistically significant difference in the means. A p-value greater than  $\alpha$  ( $p > 0.05$ ) indicates that the means are statistically the same. All reported error values are  $\pm$  the standard deviation for those values.

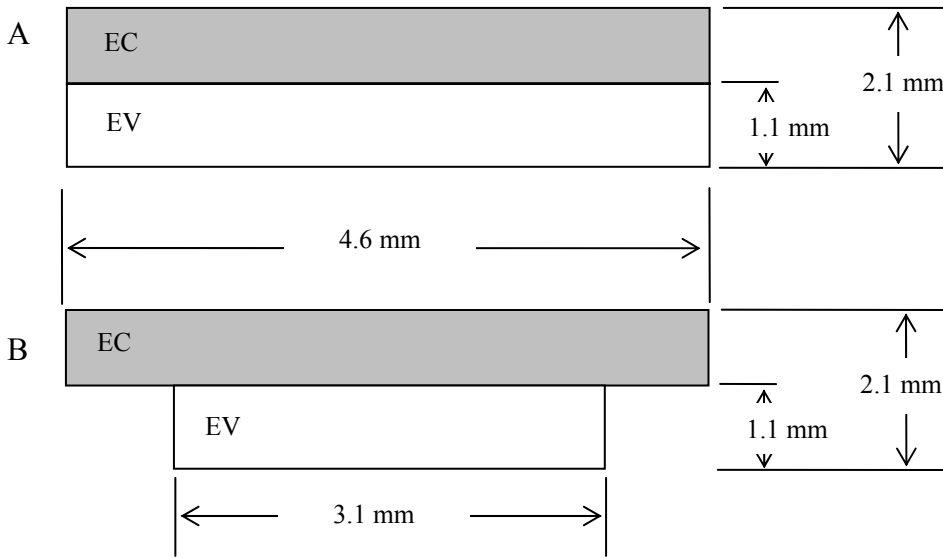


Figure 3-1. Cross-section of bilayer specimens. A) Bilayer before transformation. B) Bilayer after transformation.

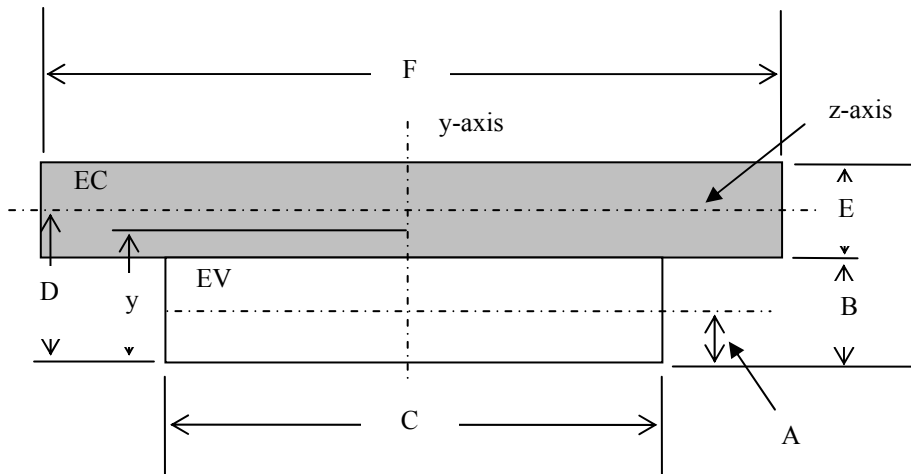


Figure 3-2. Diagram of distances used for computation of centroid for bilayer specimens.

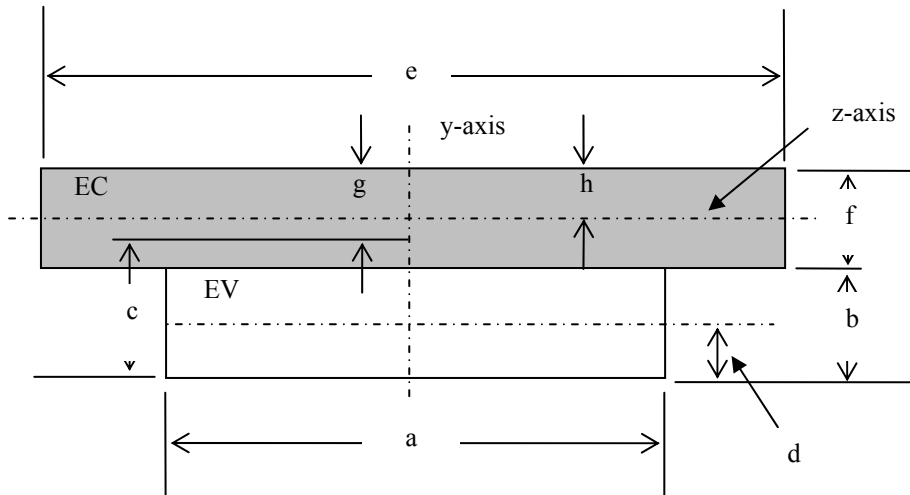


Figure 3-3. Diagram of distances used for computation of moment of inertia.

Table 3-1. Chemical composition of IPS e.max® Press [Adapted from Bühler-Zemp P, Völkel T (2005) Scientific Documentation IPS e max® Press:1]

Standard Composition	(wt. %)
SiO <sub>2</sub>	57.0 – 80.0
Li <sub>2</sub> O	11.0 – 19.0
K <sub>2</sub> O	0.0 – 13.0
P <sub>2</sub> O <sub>5</sub>	0.0 – 11.0
ZrO <sub>2</sub>	0.0 – 8.0
ZnO	0.0 – 8.0
+ other oxides	0.0 – 10.0
+ coloring oxides	0.0 – 8.0

Table 3-2. Chemical composition of IPS e.max® Ceram [Adapted from Bühler-Zemp P, Völkel T (2005) Scientific Documentation IPS e max® Ceram:1]

Standard Composition	(wt. %)
SiO <sub>2</sub>	60.0 - 65.0
Al <sub>2</sub> O <sub>3</sub>	8.0 - 12.0
Na <sub>2</sub> O	6.0 – 9.0
K <sub>2</sub> O	6.0 – 8.0
ZnO	2.0 – 3.0
+ CaO, P <sub>2</sub> O <sub>5</sub> , F	2.0 – 6.0
+ other oxides	2.0 – 8.5
+ Pigments	0.1 – 1.5

Table 3-3. AFM scan areas used to determine optimum scan areas for fractal dimension measurements of fracture surface of baria silica glass. X mark AFM scan areas used to measure fractal dimension for a given region of the fracture surface.

Scan area, ( $\mu\text{m}$ ) <sup>2</sup>	Mirror	Mist	Hackle
60	X	X	X
40	X	X	X
20	X	X	X
10	X	X	X
5	X	X	X
2	X	X	X
1	X	X	X
0.75	X	X	X
0.50	X	X	
0.30	X	X	
0.10	X		

## CHAPTER 4 RESULTS AND DISCUSSION

In this chapter, the microstructure for the dental materials is characterized. The fracture strength, apparent fracture toughness, work of fracture, and fractal dimension are determined for the monolithic dental materials and the bilayer composites. From these results, the hypotheses discussed in Chapter 1 are answered.

### **Microstructural Analysis**

#### **Phase Identification**

X-ray diffraction (XRD) was conducted for the IPS e.max® Press (EC) glass-ceramic core material and IPS e.max® Ceram EV glassy veneer. XRD was performed on the EC to determine if lithium disilicate is the main crystal in the glass ceramic. XRD was performed on the EV to determine if any crystal phases existed in the glass veneer.

The XRD data (Figure 4-1) showed that EC contains crystals. Peaks at diffraction angles of 23.9° and 24.4° correspond with two of the three highest peaks for lithium disilicate (PDF 40-0376;  $\text{Li}_2\text{Si}_2\text{O}_5$ ). This data, along with the knowledge of the fabrication of EC, confirms that EC is composed mainly of lithium disilicate crystals and is a glass-ceramics using the definition stated in Chapter 2 for glass-ceramics.

The XRD data (Figure 4-2) shows the pattern for an amorphous structure. This implies that EV may be a glass and does not contain crystals. SEM micrographs (Figure 4-3) of the veneer showed what could be nanoparticles, with a number average diameter of approximately 100 nm, that exist in the veneer. It is possible that volume fraction of the particles in the glass matrix is less than the detection limit for XRD and that this low volume fraction may be responsible for the small peaks exhibited in the XRD spectra at 25.9°, 32.0°, and 34.0°. These particles have a spherical shape when compared to the needle-like crystals reported by Ivoclar

(Figure 4-4) [6]. The difference in shape may be due to a difference in heat treatment, which would affect the growth of crystals. Work by Höland et al. has shown that temperature and time does affect crystal growth for leucite glass-ceramic, with the length of the crystals being proportional to time at elevated temperatures [62]. Energy dispersive X-ray spectroscopy (EDS) was also conducted on the veneer specimens to determine the composition of the particles (Figure 4-5). There was a smaller amount of fluorine (~ 1 wt. %) and an equivalent amount of calcium (~ 3 wt. %) present in the spectra compared to the amount reported by the manufacturer (Table 3-2). Based on the EDS and XRD data, it is inconclusive if the particles present in the veneer specimens are the nanofluorapatite crystals described by Ivoclar [6]. These findings are in agreement with the work done by Tsalouchou et al. [63] in which the nanofluorapatite crystals could not be identified for e.max® Ceram. More analysis, e.g., determine the lattice planes of the particles from TEM or determining the enthalpy of melting of the particles from DSC or TGA, is needed to determine the identity of the particle observed in SEM images.

### **Aspect Ratio**

The aspect ratio for the lithium disilicate crystals in the EC glass-ceramic was measured from SEM micrographs and compared to the aspect ratio of EC report by Holand [2] and Ivoclar [6]. Using the original etching procedure of 2.5 % HF for 10 s did not etch the glass-ceramic well enough to measure the aspect ratio (Figure 4-6). To determine the best method to etch the glass-ceramic, a 2.5 % HF solution was used to etch one polished specimen for 30 s and a 30 % sulfuric acid (H<sub>2</sub>SO<sub>4</sub>)/4 % HF solution [2] was used to etch another polished specimen for 10 s.

SEM micrographs were taken of both specimens at 5000x (Figure 4-7) and 10000x (Figure 4-7). It was determined that the H<sub>2</sub>SO<sub>4</sub>/HF solution provided the best etching to measure the aspect ratio. The aspect ratio for the lithium disilicate crystals was  $7.6 \pm 1.1$ . The number

average length for the crystals was  $5.2 \pm 2.0 \mu\text{m}$  and the number average width was  $0.7 \pm 0.3 \mu\text{m}$ . This is in agreement with the crystal lengths of 3 - 6  $\mu\text{m}$  reported by Höland [2].

### Fracture Strength

The flexural strength was determined for EC, EV, the veneer indented bilayer (BV), and the core indented bilayer (BC) to characterize and compare the dental materials and to calculate the apparent fracture toughness. In order to calculate the flexural strength for the bilayers, composite beam theory was used to transform the bilayers because of a difference in elastic modulus between the two materials. Based on the elastic moduli of the two ceramics (96 GPa for EC [52] and 64 GPa for EV [52]), the transformation factor was calculated to be 1.5. This transformation factor results in a virtual change in the width of EV from 4.6 mm to 3.1 mm (Figure 3-1). Using Equation 3-2 and Figure 3-2,  $y$  was determined for the BV ( $\sim 1.14 \text{ mm}$ ) and BC ( $\sim 0.94 \text{ mm}$ ).

Using Equation 3-3 and Figure 3-3, the average moment of inertia was calculated to be  $2.7 \text{ mm}^4$ . Using the calculated moment of inertia, Equation 3-4 and 3-5,  $\sigma$  was calculated for each bilayer (Table 4-1).

The measured flexural strength of EC is greater than that of EV. This is expected for the EC due to the presence of the needle-like lithium disilicate crystals that increases the strength of the materials due to crack deflection. It is expected that the fracture strength of both bilayers will have a flexural strength greater than EV and less than EC based on the Rule of Mixtures [64]. Using the Rule of Mixtures, the fracture strength of the bilayer ( $\sigma_B$ ) was determined from the equation

$$\sigma_B = \sigma_{EV} A_{EV} + \sigma_{EC} A_{EC} \quad (4-1)$$

where  $\sigma_{EV}$  is the fracture strength of the veneer,  $A_{EV}$  is the area fraction of the veneer in the bilayer,  $\sigma_{EC}$  is the fracture strength of the core, and  $A_{EC}$  is the area fraction of the core. Using Equation 4-1 implies that the strength of each layer can be superimposed to determine the strength of the composite beam. For the bilayer,  $\sigma_B = 94$  MPa. This shows that the fracture strength of the bilayers should be between the values for the fracture strength of the veneer and core. Table 4-1 shows that the fracture strength for BV and BC does lie between the fracture strength of the veneer and core. Therefore, this implies that the location of the crack determines the fracture strength of the bilayer.

### **Fracture Toughness**

The apparent fracture toughness ( $K_C$ ) was determined for EC, EV, and the two sets of bilayers (BV and BC) to compare to measured values reported in the literature. The apparent fracture toughness was determined using two methods: strength indentation and fractography. From Equation 3-6 and 3-7,  $K_C$  was calculated for each method and displayed in Table 4-1. For Equation 3-7, the elastic modulus and hardness used was 64 GPa [3] and 5.4 GPa [6] for EV and 96 GPa [3] and 5.5 GPa [6] for EC. Both sets of  $K_C$  values for EC agree with the values reported by Ivoclar [6] and are statistically similar ( $p > 0.05$ ). Both sets of the apparent fracture toughness values for EV are not statistically the same ( $p < 0.05$ ) but are within the range of the  $K_C$  value reported by Taskonak [4]. The difference in the mean of the apparent fracture toughness for the bilayers was not statistically significant ( $p > 0.05$ ).  $K_C$  for the bilayers was greater than  $K_C$  for the veneer monolithic specimens and less than that for the core monolithic specimens. The implication of these results is that the apparent fracture toughness of a bilayer is dependent on the location of crack initiation in the bilayer. Therefore, if the initiating crack is in the veneer, then the fracture toughness of the veneer controls the strength and toughness of the composite.

## Work of Fracture

### Soda-Lime-Silica Glass

The work of fracture ( $\gamma_{\text{WOF}}$ ) was determined for EC, EV, and the two sets of bilayers to determine if the fracture energy could be estimated for the dental ceramics. The work of fracture was calculated in two different ways: using the cross-sectional area  $\gamma_{\text{WOF(CS)}}$  (Equation 2-1) and using the actual fracture surface area  $\gamma_{\text{WOF(F)}}$  (Equation 3-10). In order to test the accuracy of using Equation 3-10 to estimate the fracture energy of a brittle material,  $\gamma_{\text{WOF}}$  was determined for soda-lime-silica (SLS) glass for unstable and stable crack growth.

An atomic force microscope (Dimension 3100, Veeco Instruments Inc., Woodbury, NY) was used to determine the actual fracture surface area of the SLS glass beams. Using the AFM software, the surface area was determined from a grid of triangles of a fixed side length, equal to the distance between pixels, placed over the scan image. The area of all the triangles was measured and all of the areas were added together to calculate the surface area for the image. Five square scan areas ( $(1 \mu\text{m})^2$ ,  $(750 \text{ nm})^2$ ,  $(500 \text{ nm})^2$ ,  $(375 \text{ nm})^2$ , and  $(250 \text{ nm})^2$ ) were used to measure the fracture surface area for the CN specimens while four [ $(500 \text{ nm})^2$ ,  $(150 \text{ nm})^2$ ,  $(50 \text{ nm})^2$ , and  $(25 \text{ nm})^2$ ] were used to measure the unstable fracture specimens. All scans were conducted using a tapping tip at a scan rate of 3-4 Hz and at a resolution of 512 lines per scan. Equation 3-13 was used to determine the fracture surface area. Examples of the AFM scan images of the mirror, mist, and hackle region are illustrated in Figure 4-10.

The fracture surface area versus the scan area was graphed for the stable crack growth chevron-notched (CN) (Figure 4-11), and the unstable indented specimens (Figure 4-13), to determine if a relationship existed between the two variables. A number of curve fits were applied to all the data. The best fit was to a power law relationship, i.e.,

$$A_F = A\eta^{-B} \quad (4-2)$$

where  $\eta$  is the scan area side length, and A and B are constants, existed between the scan area and  $A_F$ . Equation (4-2) is similar to the profile length measurement equation (Equation 2-3) and the direct area measurement equation (Equation A-8). It is assumed here that fracture surfaces are fractal in nature, in agreement with many studies in the literature [38-40, 42-47]. Therefore, Equation 4-3 would be expected to be similar to Equations 2-3 and A-8, since the fracture surfaces are fractal. Based on this, the fracture surface area should increase as the scan area side length decreases.

In order to determine the actual fracture surface for a specimen, a maximum  $A_F$  must be determined for that specimen. Since there is no mathematical limit for Equation 4-2, a physical limit is necessary based on some physical restraints. There are three possible solutions for the size limitation: probe tip radius, equilibrium bond length, and the free volume diameter.

The physical limit for determining  $A_F$  is based on the AFM probe tip radius. The AFM can only resolve features equal to or greater than the tip radius. For the tapping tip used in these scans, the tip radius was 8-10 nm. Using the tip radius of 8 nm as  $\eta$  results in an  $A_F$  of  $6.3 \pm 0.3$  mm<sup>2</sup> (Figure 4-12).

Theoretically, a minimum limit could be the equilibrium bond length for the materials. For the soda-lime-silica glass, which is composed mostly of silica, the equilibrium bond length selected was that of Si-O, which is 0.16 nm [65]. Using the equilibrium bond length as  $\eta$  generates an  $A_F$  of  $7.1 \pm 0.5$  mm<sup>2</sup> (Figure 4-12).

Another limit is based on the concept of free volume. Inorganic glasses have open space due to the disorder in the glassy structures. These open spaces are known as free volume. Swiler et al [66] suggested from molecular dynamics calculations that it was these free volume areas

that controlled fracture in silica glass. The estimated size of the region was represented by a radius,  $a_0$ . West et al. [44] also estimated this region using a different approach.  $a_0$  was determined to be approximately 1.2 nm. The projection of  $A_F$  based on AFM measurements at a  $\eta$  of  $a_0$  is  $6.7 \pm 0.4 \text{ nm}^2$  (Figure 4-12). Using these three limits, Figure 4-12 shows that the fracture surface area does increase as the side length of the scan area decreases and that the fracture surface area is larger than the cross-sectional area.

Using the three previously mentioned limits,  $\gamma_{\text{WOF}}$  was calculated for the CN specimens. From Table 4-2, all the values are less than the value for  $\gamma_{\text{WOF}}$  measured using  $A_{\text{CS}}$  (Equation 2-1) and for the fracture energy measured from traditional fracture mechanics tests [ $\gamma = 3.5 \text{ J/m}^2$ ] [67]. The selection of the limit does not greatly affect the results. There is only a 13 % change for  $\gamma_{\text{WOF}}$  between using the tip radius and the equilibrium bond length. Thus, our choice of limits is not critical to determining  $\gamma_{\text{WOF}}$ , just that there is a cutoff length of atomic dimensions.

Using the equilibrium bond length as the limit for the scan area side length,  $A_F$  was determined for the unstable crack growth specimens (Table 4-3) by extrapolating to the equilibrium bond length. The values for  $\gamma_{\text{WOF(AF)}}$  are similar to the theoretical fracture energy ( $\gamma$ ) for fused silica of  $1.75 \text{ J/m}^2$  calculated by Charles [65] based on the equilibrium bond length of silica and less than the fracture energy measured from traditional fracture mechanics test [ $\gamma = 3.5 \text{ J/m}^2$ ] [67]. The results of both experiments confirmed that the actual fracture surface area provides a lower limit of the work of fracture and that the fracture energy required to break bonds can be estimated using the work of fracture.

To obtain an accurate value for the fracture energy, the entire fracture surface generated during crack growth should be measured or estimated. This further implies that for any fracture surface generated during fracture, the actual fracture surface area should be measured or

estimated to obtain a more accurate value of the energy required to break atomic bonds. The experiments also show that because of the lower limit, using traditional fracture mechanics tests to calculate  $\gamma$  do not represent the minimum energy needed to rupture an atomic bond and create the fracture surface.

### **Dental Materials**

After showing that  $\gamma_{\text{WOF(F)}}$  can be used to estimate the fracture energy of SLS glass, the fracture surfaces of EC, EV, and the two sets of bilayers were measured using the AFM to determine if the fracture energy could be estimated for these materials. The crack introduced in the veneer and core monolithic specimens, from Vickers indentation, resulted in a fracture surface with no mist or hackle present on the surface. Therefore, only the mirror portion of Equation 3-13 was necessary to calculate  $A_F$  for the specimens and  $N(\text{SS})$  is equal to the cross-sectional area of the bars.

Using the same method to determine  $\gamma_{\text{WOF(AF)}}$  in the SLS glass specimens, the scan areas were graphed versus the fracture surface area for EV (Figure 4-14) and EC (Figure 4-15) over scan areas of  $(250 \text{ nm})^2$  to  $(25 \text{ nm})^2$ . Since the veneer and the core consisted mainly of silica, the equilibrium bond length of silica [0.16 nm] was used in determining the minimum scan area. Based on the scan areas used,  $\gamma_{\text{WOF(F)}}$  for EV was  $5.2 \pm 1.4 \text{ J/m}^2$  and  $33 \pm 17 \text{ J/m}^2$  for EC. Although these two values are significantly greater than the theoretical value for silica of  $1.75 \text{ J/m}^2$ , the values are less than the values reported for  $\gamma_{\text{WOF(CS)}}$  (Table 4-4). The values for  $\gamma_{\text{WOF(F)}}$  may be due to the small sampling of fracture surface area ( $A_F$ ) determined from the AFM data. On further analysis,  $A_F$  for the veneer and core appears to have a different level of roughness on a scale of hundreds of micrometers. To see if the roughness increases  $A_F$  of the veneer and core, the fracture surface of the two materials was measured using an optical profilometer (WYKO NT1000, Veeco Metrology Group, Tucson, AZ). The fracture surface was examined at two

different scan areas: 0.270 mm<sup>2</sup> (objective lens of 5x and field of view lens of 2x) and 0.503 mm<sup>2</sup> (objective lens of 5x and field of view lens of 1.5x). The scan area of 0.270 mm<sup>2</sup> resulted in A<sub>F</sub> being 13 % greater than the cross-sectional area (A<sub>CS</sub>) measured for the veneer and 28 % greater for the core. For the scan area of 0.503 mm<sup>2</sup>, there was a 10 % increase in A<sub>F</sub> for the veneer and a 21 % increase in A<sub>F</sub> for the core. Using the data from the large scan area and applying this information to the data acquired from the AFM,  $\gamma_{\text{WOF(F)}}$  decreased to  $2.9 \pm 0.8 \text{ J/m}^2$  for the veneer and  $26.1 \pm 13.4 \text{ J/m}^2$  for the core.

Although there was a decrease in  $\gamma_{\text{WOF(F)}}$ , it is still greater than that of the theoretical value for silica. One likely cause for the larger  $\gamma_{\text{WOF(F)}}$  values is the speed of the crack for the unstable crack growth specimens. The speed of the crack does not allow the crack to follow the path of lowest energy. This results in more energy being supplied than what is required to fracture a material when compared to the fracture surface area created during fracture, i.e.,

$$\frac{\partial U}{\partial A} > \gamma \quad (4-1)$$

where U is the elastic energy stored in system and A is the fracture surface area [24]. But, since the crack velocity was not measured for the specimens, it is inconclusive if the crack velocity affects the fracture surface area.

After  $\gamma_{\text{WOF}}$  for the monolithic dental ceramics,  $\gamma_{\text{WOF}}$  for the veneer-indented (BV) and core-indented bilayer (BC) was calculated using the same method as for the monolithic materials. The scan area side length versus A<sub>F</sub> was plotted for BV (Figure 4-16) and for BC (Figure 4-13). For BV,  $\gamma_{\text{WOF(F)}}$  is  $5.6 \pm 1.4 \text{ J/m}^2$  and for BC it is  $25 \pm 6 \text{ J/m}^2$ . These values follow the trend of the values for the fracture strength and apparent fracture toughness, with  $\gamma_{\text{WOF}}$  for BV being greater than that for EV and  $\gamma_{\text{WOF}}$  of BC being less than that for EC. Although optical profilometry was not used in determining A<sub>F</sub> for the bilayers,  $\gamma_{\text{WOF}}$  for BV and BC would

decrease based on the results from the measurement of  $A_F$  on the monoliths. Based on the values for  $\gamma_{WOF(F)}$  for the bilayers, it was shown that  $\gamma_{WOF(F)}$  is similar to that of the material in which the initial crack that caused fracture of the bilayer is located. For fracture in the bilayer, in which fracture initiated in the tougher material (core),  $\gamma_{WOF(F)}$  is similar to that of the tougher monolith (core). For fracture in the bilayer, in which fracture initiated in the less tough material (veneer),  $\gamma_{WOF(F)}$  is similar to that of the less tough monolith (veneer). These results based on  $\gamma_{WOF(F)}$  further indicate that selection of both materials in a bilayer is important when designing ceramic composites.

## **Fractal Dimension**

### **Soda-Lime-Silica Glass**

The fractal dimension (D) of e.max® Press (EC), e.max® Ceram (EV), and the two set of bilayers of EC/EV were measured using an AFM and the two software packages of Gwyddion and WSxM to determine if location of crack initiation changes D for the veneer and core in the bilayers. To determine the accuracy of D measurements using these two programs, D was measured for soda-lime-silica (SLS) glass bars. Three SLS bars (45mm x 4mm x 3 mm) were indented with a Vickers indent load of 2 kgf and fractured under four-point flexure at a crosshead speed of 0.5 mm/min. The mirror, mist, and hackle regions of the fracture surface were scanned using 6 scan areas [(100 nm)<sup>2</sup>, (250 nm)<sup>2</sup>, (375 nm)<sup>2</sup>, (500 nm)<sup>2</sup>, (750 nm)<sup>2</sup>, and (1 $\mu$ m)<sup>2</sup>].

Table 4-5 shows the fractal dimension increment (D\*) values calculated from the two programs. For the Gwyddion software, only the triangulation method and the cube counting method were used to measure D\*. The variance and power spectrum methods were not used because there was too much scatter in the data points used to determine the slopes, producing inconsistency in the D\* values calculated for these methods. The difference in mean values between the Gwyddion and WSxM software were not statistically significantly for the hackle

region ( $p > 0.05$ ). For Gwyddion, the triangulation and cube counting were significantly similar for the mist and hackle region but not for the mirror region (Table 4-5).

The mist and hackle values agree with a  $D^*$  of  $0.10 \pm 0.01$  for glasses [61, 68] determined using the slit island method. Thompson et al. [69] showed that for a lithia-disilicate ceramic, determining  $D^*$  from the slit-island method and AFM results in the same value of 0.23. Both the Gwyddion and WSxM software showed an increase in  $D^*$  for the mirror region when compared to  $D^*$  for the mist and hackle regions. Kulawansa [38] had conducted work on measuring  $D$  of SLS glass near the mirror-mist boundary. His work determined that  $D^*$  was  $0.17 \pm 0.08$  with some values in the rougher regions as high as 0.40. If the fractal dimensions of the three regions measured using the Gwyddion and WSxM software are averaged, the values for the Gwyddion software [Triangulation -  $0.18 \pm 0.10$ ; cube counting -  $0.17 \pm 0.09$ ] agree with Kulawansa's measured value for  $D^*$  while WSxM [ $0.30 \pm 0.25$ ] does not.

Although WSxM produces a greater  $D^*$  value for the mirror region, the key point is that the fractal dimension of the mirror region is greater than the fractal dimension of the mist or hackle region. This may be due to the roughness in the mirror region being less than that in the mist or hackle region. Wiederhorn et al. [70] showed that for the mirror region of SLS glass, the root-mean-square (RMS) roughness decreased as the crack velocity increased. The roughness exponent, which is related to the fractal dimension, also increased as the RMS roughness decreased for SLS glass. These results imply that the increase in the  $D^*$  for the mirror region is not due to any algorithm errors in Gwyddion or WSxM, but rather due to a change in the material itself.

To further examine if the greater  $D^*$  values for the mirror region measured using the software program is due to the algorithms used in the programs, five line profiles from five AFM

scans  $[(1\mu\text{m})^2, (750\text{ nm})^2, (500\text{ nm})^2, (375\text{ nm})^2, \text{ and } (250\text{ nm})^2]$  for the mirror region of SLS glass were used to determine  $D^*$ . The Richardson's method was used to measure  $D^*$  by measuring the length of each profile as a function of step size (50, 40, 30, 20, and 10 nm).  $D^*$  from the profiles was  $0.35 \pm 0.08$ . This value is similar to the values measured using the triangulation and cube counting method. This shows that  $D^*$  determined from the algorithms used to calculate  $D^*$  in Gwyddion do not result in a significant change in the  $D$ . Based on this, it was determined that the increase in the  $D^*$  values for the mirror region is not caused by the software programs used to calculate  $D^*$ .

Along with greater value for  $D^*$  for the mirror region calculated from the WSxM software, there are several other problems with using WSxM. The number of variables that are used in calculating  $D^*$ , e.g., the height of the sectioning plane and the minimum island area, results in an inconsistency in the calculation of  $D^*$ . The island area and number of islands that is necessary to accurately calculate  $D^*$  has not been determined for WSxM. Based on this, WSxM was not used as a tool to measure the fractal dimension of the brittle materials in this study. All fractal dimension values reported from this point on were determined from the Gwyddion software program.

### **Baria Silica Glass**

Using Gwyddion as the software to measure  $D^*$ , the effect of AFM scan areas on  $D^*$  was tested. Baria silica glass ( $3\text{BaO}\cdot 5\text{SiO}_2$ ) bars (25mm x 4 mm x 2 mm) were used in this experiment since baria silica glass has the same fractal dimension as other glasses [ $0.10 \pm 0.01$ ] [61]. The baria silica bars were fractured in three-point flexure, at a crosshead speed of 0.5 mm/min., using a Vickers indent of 500 gf to initiate a crack. The fractal dimension was determined for the fracture surface of the mirror, mist, and hackle regions at different scan areas

from  $(100 \text{ nm})^2$  to  $(60 \text{ }\mu\text{m})^2$  and compared to  $D^*$  calculated from the slit-island technique [ $0.10 \pm 0.01$ ] [61].

Figure 4-17 confirms that  $D^*$  does change when the scan area change. The fractal dimension increment decreases as scan area decreases for the mirror, mist, and hackle region. As the scan area increases, the time it takes for the tip to scan a line increases causing a decrease in the time the tip has to measure the features of the fracture surface. This results in a decrease in resolution and a decrease in the measurement of the surface area. The measurement of the surface area using AFM is also limited by the tip radius of the probe. The probe can only resolve features that are larger than the tip radius. Based on this data, scan areas less or equal to  $(750 \text{ nm})^2$  for the mirror region, less than  $(2\text{ }\mu\text{m})^2$  for the mist region, and between  $(1 \text{ }\mu\text{m})^2$  and  $(20 \text{ }\mu\text{m})^2$  for the hackle region would be the ideal scan areas used to measure the fracture surface for glasses using AFM.

### **Dental Materials**

With the limits of the AFM determined for  $D^*$  measurements,  $D^*$  was measured for the e.max® Press (EC) and e.max® Ceram (EV) monolithic bars as a control group in order to establish if a change in  $D^*$  exist in the bilayer bars. The fracture surfaces (Figure 4-18) of the three bars each of EC and EV were measured at 250, 375, 500, 625, and 750  $(\text{nm})^2$  to determine  $D^*$ . Table 4-6 shows the average  $D^*$  for the dental core and veneer.  $D^*$  values for the veneer are similar to that of SLS and baria silica glass. This is expected for the veneer since it is mostly glass, based on the previous XRD analysis, and the fracture surface is all mirror. Therefore, the veneer should have a fractal dimension similar to that of the mirror region of other silicate-based glasses. The fractal dimension for the core was less than  $D^*$  values reported for other lithia-disilicates [0.25 [71], 0.24 [69]]. This difference in  $D^*$  may be caused by a difference in the microstructure of the lithia-disilicates, a difference in the scale at which  $D^*$  was calculated for

the lithia-disilicates compare to the scale used in this experiment, or that the fracture surface of the core is mostly mirror for EC and different from the fracture surface of the other glass-ceramics. Thompson [69] measured  $D^*$  for fully crystallized lithia-disilicate. The amount of crystallinity may have resulted in the greater value in  $D^*$ . Naman [72] measured the fractal dimension of lithia-disilicate glass and lithia disilicate glass-ceramic at 10, 33, and 95 vol. % crystallinity using the slit-island method. Naman showed that for the mirror region,  $D^*$  was 0.03 in the glass, 0.05 in the 10 vol. % glass-ceramic, 0.09 in the 33 vol. % glass-ceramic, and 0.16 in the 95 vol. % glass-ceramic. The value for the 33 vol. % glass-ceramic agree with the values for the core (EC). Therefore, the difference in the  $D^*$  measurements is mostly like due to the fracture surface of the core (EC), which has a fracture surface that is mostly mirror. Future investigations should be conducted to determine the cause of the fractal dimension values for the ceramics in the mirror region. One direction to explore for future research is the effect that the crack velocity has on the fractal dimension.

There was no significant difference ( $p > 0.05$ ) for either the cube counting or triangulation values at the different scan areas. This means that  $D^*$  was not affected for the range of scan areas used. The cube counting and triangulation values for EV and EC were not significantly similar ( $p \leq 0.05$ ) to each other though. As Table 4-4 shows,  $D^*$  from triangulation is greater than the cube counting values. This is because there is a better linear fit to the data used to calculate  $D^*$  for cube counting than triangulation resulting in a lower but more accurate calculation of  $D^*$  from cube counting.

With the  $D^*$  values determined for the monolithic materials,  $D^*$  was calculated for the bilayers to determine if  $D^*$  changes in the material in which the initial crack is not located. The fracture surfaces of the three veneer-indented bilayer bars (BV) and three core-indented bilayer

bars (BC) was measured at 250, 375, 500, 625, and 750 (nm)<sup>2</sup> to determine D\*. Table 4-7 shows the average D\* for BV and BC. The difference in the means of triangulation and cube counting D\* values for the veneer and core materials in the BV and BC bilayers were statistically different ( $p < 0.05$ ). As previously mentioned, this is due to how D\* is calculated for the triangulation and cube counting methods. For BV and BC bilayers, D\* for the veneer and core were statistically similar ( $p > 0.05$ ) to D\* for the monolithic veneer and core. As mentioned previously, D\* for the core was different from D\* determined from other researchers. Although the D\* values were different, the key point is that D\* is the same for the core materials in the bilayers and in the monolith.

To determine if the crack propagation was continuous or if a new crack initiated and propagated in the non-indented materials in the bilayer, SEM was used to examine the interface of the bilayer. Figure 4-19 shows examples of the fracture surface of the veneer-indented bilayer (BV). Figure 4-19B indicates that the wake hackle marks generated by the pores in the veneer layer, which are due to processing, travel through the interface into the core. This observation confirms that the materials in the bilayer were bonded well since there was no indication of delamination or secondary crack initiation at the interface. Thus, the fracture process was continuous from the veneer, where the indented induced flaw is located on the tensile surface, into the core material. Figure 4-20 shows examples of the fracture surface of the core-indented bilayer (BC). Figure 4-20B shows twist hackle marks present in the veneer at the interface. The presence and direction of these twist hackle marks indicate that the crack propagated continuously through the bilayer, starting in the tensile surface of the core-indented layer and propagating across the interface into the veneer.

Based on the  $D^*$  information for the bilayers, the location of crack initiation and propagation does not change the fractal dimension of either of the materials in the bilayer when compared to their monolithic counterparts. This means that the fracture surface of the materials did not change based on the location of initial crack initiation. This confirms that for the ceramic bilayer specimens tested in flexure, the fracture process does not change the fractal dimension of the material in which the initial indented-induced flaw is not located. The fact that the fracture surface of the ceramic materials does not change supports the idea that the fractal dimension is an intrinsic property of the material. With the fractal dimension being shown to be a property of the material and not determined by the fracture process, the fractal dimension can be used as another property to describe fracture in the ceramic materials.

Table 4-1. Fracture strength, fracture toughness determined from strength indentation (SI), and fracture toughness determined from fractography (F) for e.max® Ceram (EV), e.max® Press (EC), bilayer with crack initiation in veneer (BV), and bilayer with a flaw produced in the core (BC)

Specimen	No. of Specimens	$\sigma$ , MPa	$K_C$ (SI), MPa·m <sup>1/2</sup>	$K_C$ (F), MPa·m <sup>1/2</sup>
EV	5	49 ± 3	0.83 ± 0.04	0.74 ± 0.07
EC	5	155 ± 23	2.46 ± 0.27	2.25 ± 0.34
BV	5	67 ± 11	1.14 ± 0.07	1.21 ± 0.14
BC	4	142 ± 15	2.30 ± 0.18	2.25 ± 0.18

Table 4-2. Work of fracture values calculated for chevron notch specimens using cross-sectional area (ACS) and actual fracture surface area based on probe tip radius, equilibrium bond length, and free volume  $a_0$ . Actual area is projected area using equilibrium bond length.

Cross-sectional area (mm <sup>2</sup> )	Actual area (mm <sup>2</sup> )	$\gamma_{\text{WOF}}$ (for ACS) (J/m <sup>2</sup> )	$\gamma_{\text{WOF}}$ (Tip Radius) (J/m <sup>2</sup> )	$\gamma_{\text{WOF}}$ (Bond Length) (J/m <sup>2</sup> )	$\gamma_{\text{WOF}}$ ( $a_0$ ) (J/m <sup>2</sup> )
5.4 ± 0.3	7.1 ± 0.5	3.5 ± 0.1	3.0 ± 0.1	2.7 ± 0.2	2.6 ± 0.2

Table 4-3. Comparison of work of fracture and fracture toughness, based on work of fracture, for unstable crack growth soda-lime-silica glass specimens

	No. of specimens	Actual Area (mm <sup>2</sup> )	W, mJ	$\gamma_{\text{WOF}}$ (ACS), J/m <sup>2</sup>	$\gamma_{\text{WOF}}$ , J/m <sup>2</sup>	$K_C$ , MPa·m <sup>1/2</sup>
3 mm	7	860 ± 76	2.7 ± 0.6	113 ± 30	1.6 ± 0.4	0.46 ± 0.06
10 mm – 1000 gf	7	4002 ± 161	8.0 ± 2.0	74 ± 12	0.9 ± 0.1	0.35 ± 0.02
10 mm – 2000 gf	8	4438 ± 98	6.5 ± 0.8	57 ± 7	0.8 ± 0.1	0.32 ± 0.02

Table 4-4. Work of fracture  $\gamma_{\text{WOF}}$ , based on cross-sectional area ( $A_{\text{CS}}$ ) and fracture surface area ( $A_{\text{F}}$ ) for veneer, core, and bilayer bars

Specimen	No. of specimens	W, mJ	$\gamma_{\text{WOF}}$ ( $A_{\text{CS}}$ ), J/m <sup>2</sup>	$\gamma_{\text{WOF}}$ ( $A_{\text{F}}$ ), J/m <sup>2</sup>	$\gamma_{\text{WOF}}$ (Adj. $A_{\text{F}}$ ), J/m <sup>2</sup>
EC	3	3.9 ± 1.2	212 ± 63	33 ± 17	26.1 ± 13.4
BC	3	3.6 ± 0.7	190 ± 37	25 ± 6	
EV	3	0.6 ± 0.1	31 ± 4	5.2 ± 1.4	2.9 ± 0.8
BV	3	0.9 ± 0.3	49 ± 16	5.6 ± 1.4	

Table 4-5. Fractal dimensional increment for soda-lime-silica glass fracture surface regions measured using atomic force microscopy and the Gwyddion and WSxM software

Fracture Surface Region	Gwyddion Triangulation	Gwyddion Cube counting	WSxM
Mirror	$0.29 \pm 0.05$	$0.26 \pm 0.05$	$0.60 \pm 0.19$
Mist	$0.13 \pm 0.07$	$0.12 \pm 0.06$	$0.19 \pm 0.12$
Hackle	$0.12 \pm 0.06$	$0.11 \pm 0.06$	$0.10 \pm 0.07$

Table 4-6. Fractal dimensional increment for e.max® Ceram (EV) and the e.max® Press (EC) ceramics measured using AFM and Gwyddion software

Specimen	Triangulation	Cube Counting
EV	$0.27 \pm 0.11$	$0.22 \pm 0.09$
EC	$0.12 \pm 0.04$	$0.09 \pm 0.03$

Table 4-7. Fractal dimensional increment for bilayer specimens using AFM and Gwyddion

Specimen	Triangulation	Cube Counting
Veneer Indented (BV)		
EV	$0.29 \pm 0.07$	$0.22 \pm 0.06$
EC	$0.12 \pm 0.05$	$0.10 \pm 0.04$
Core Indented (BC)		
EV	$0.31 \pm 0.10$	$0.24 \pm 0.08$
EC	$0.12 \pm 0.03$	$0.09 \pm 0.03$

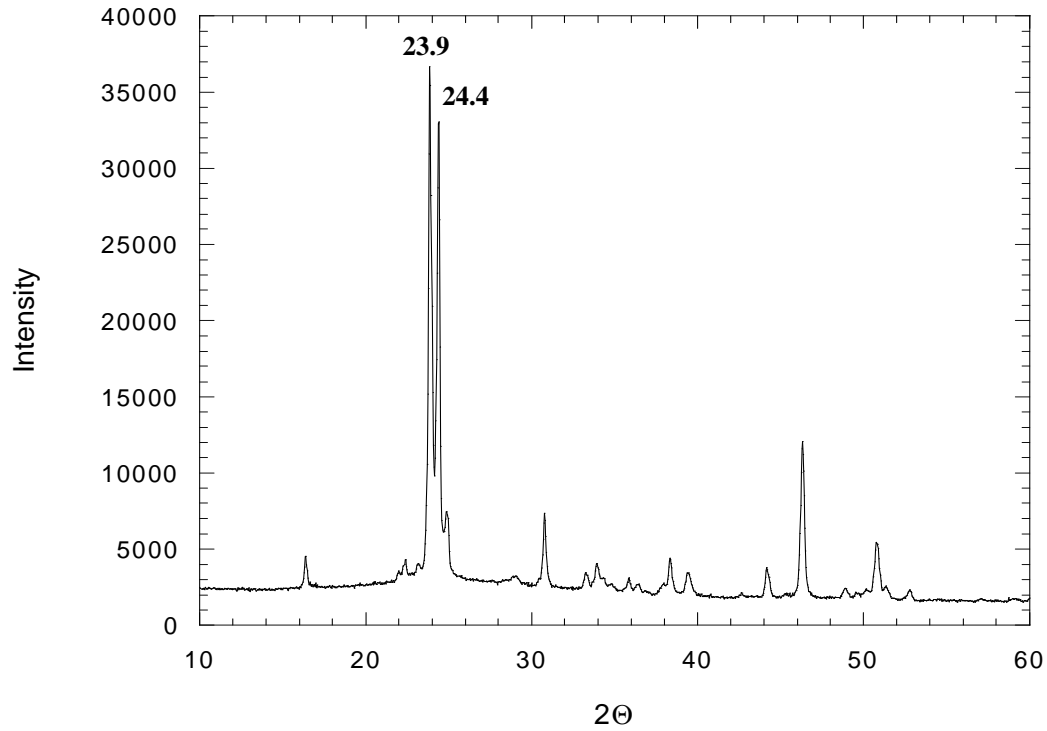


Figure 4-1. X-ray diffraction pattern for e.max® Press (EC) core ceramic showing that lithium disilicate are the crystals present in the glass-ceramic. Peaks at diffraction angles of 23.9° and 24.4° correspond with two of the largest peak intensity values for lithium disilicate (PDF 40-0376).

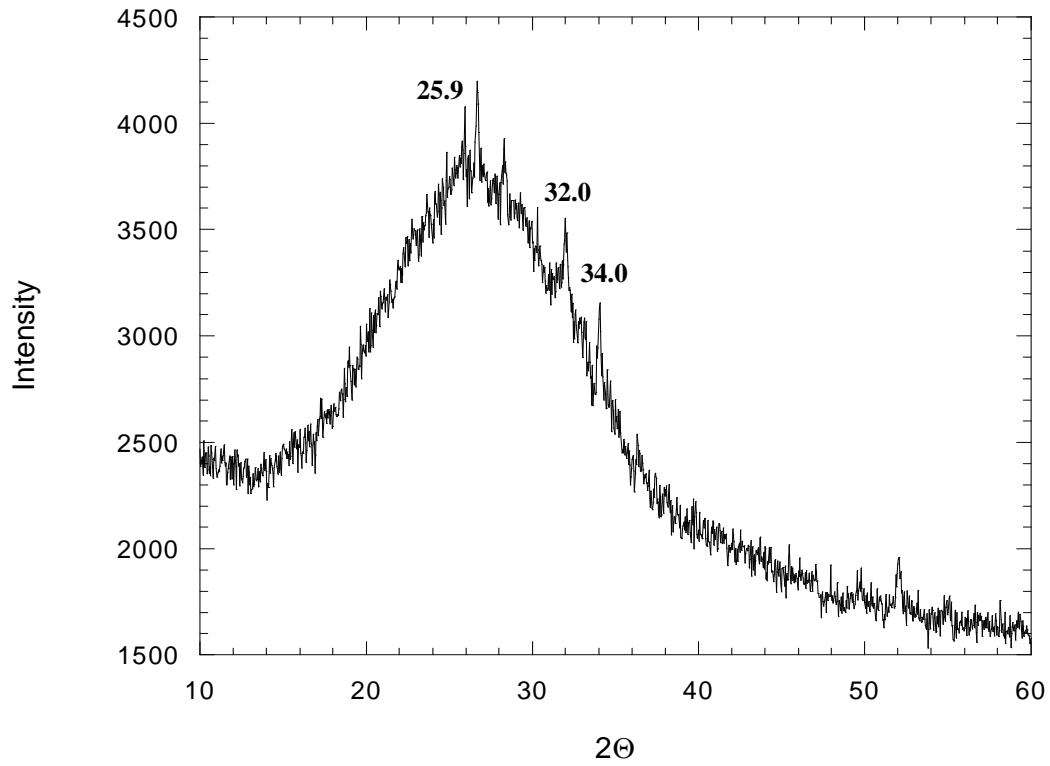
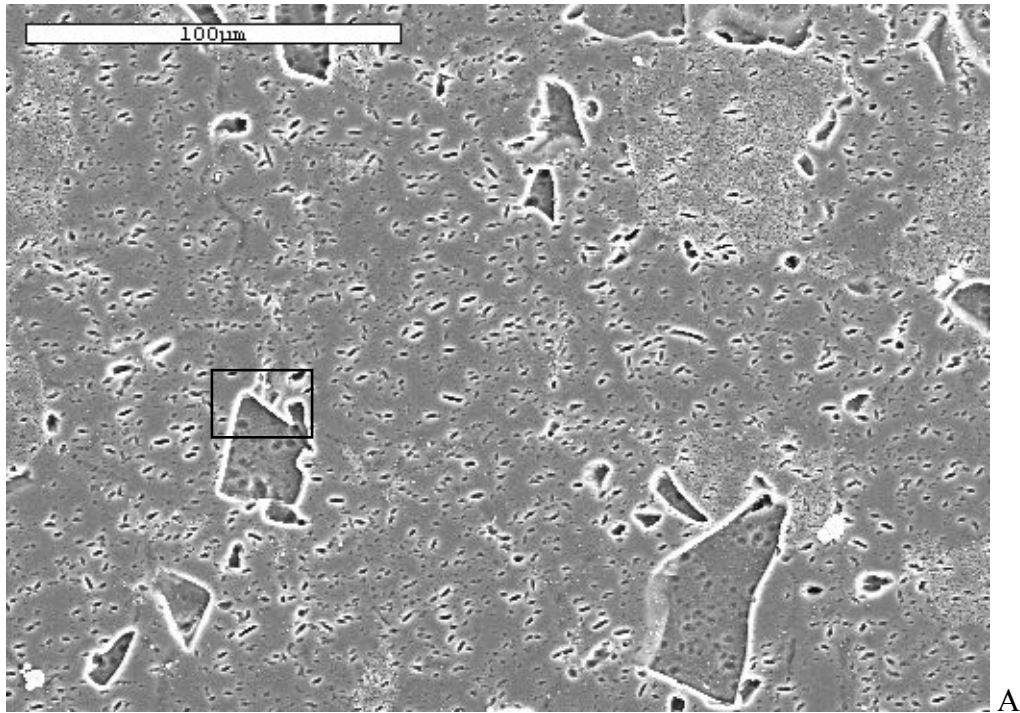
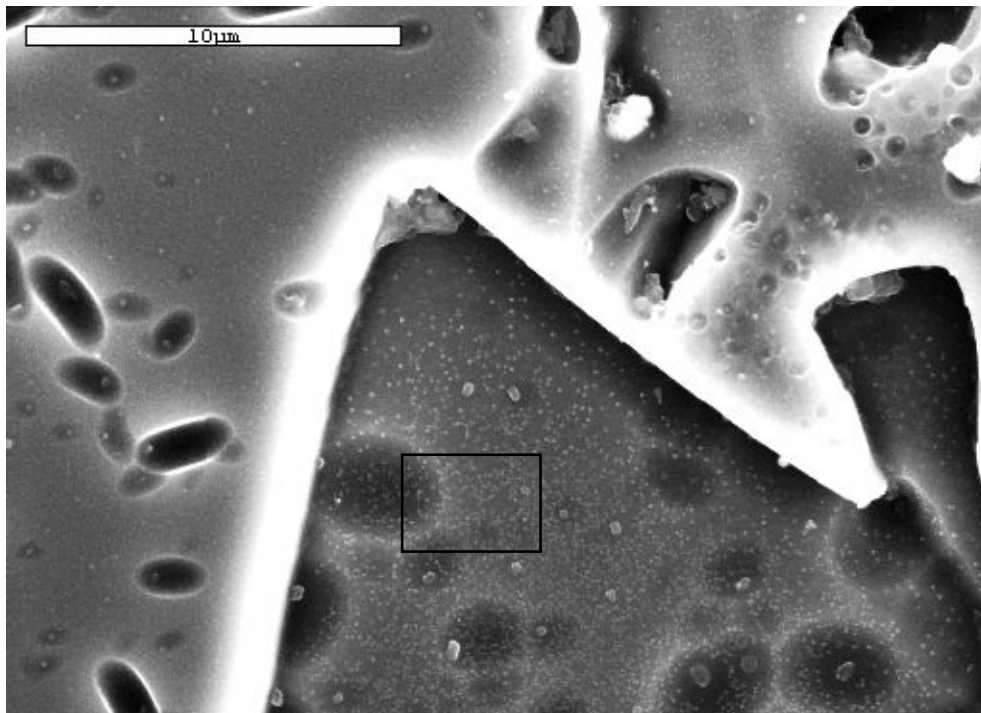


Figure 4-2. X-ray diffraction pattern of e.max® Ceram (EV) veneer ceramic showing veneer material has an amorphous pattern. Peaks in pattern at diffraction angles of 25.9°, 32.0°, and 34.0° could represent peaks for calcium fluoride phosphate (PDF 15-0876).



A



B

Figure 4-3. SEM micrographs of polished and etched surface of e.max Ceram (EV) veneer ceramic. Surface etched using 2.5 % HF solution for 10s. A) Magnification of surface at 500x. B) Magnification of box in Figure 4-3A at 5000x. C) Magnification of box in Figure 4-3B, at 30000x, showing presence of nanoparticles.

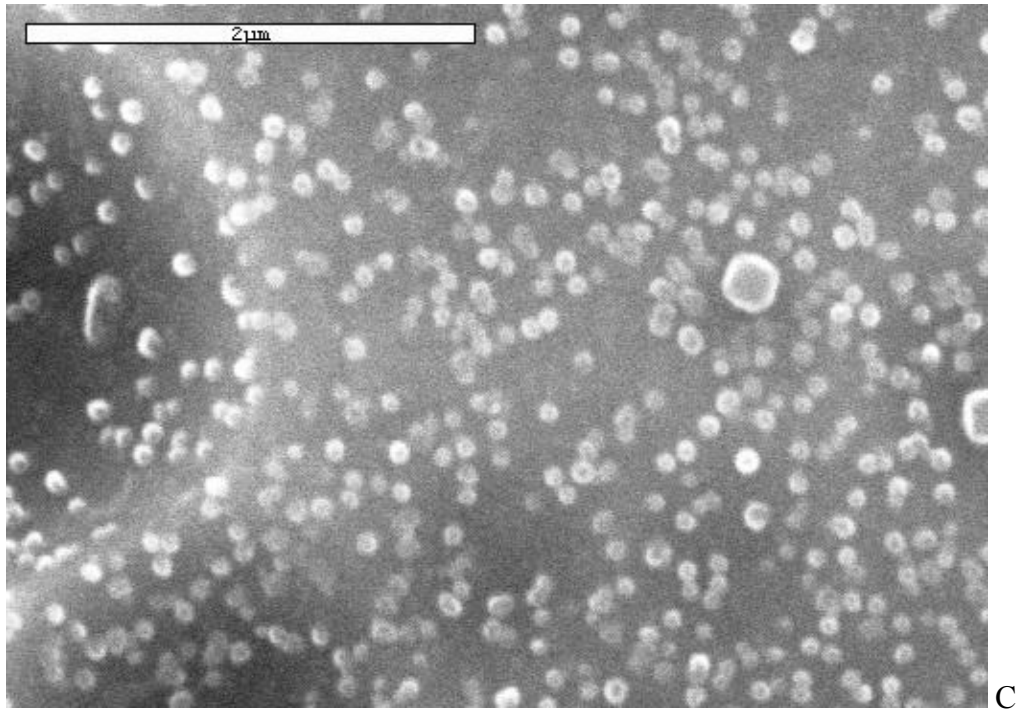


Figure 4-3. Continued

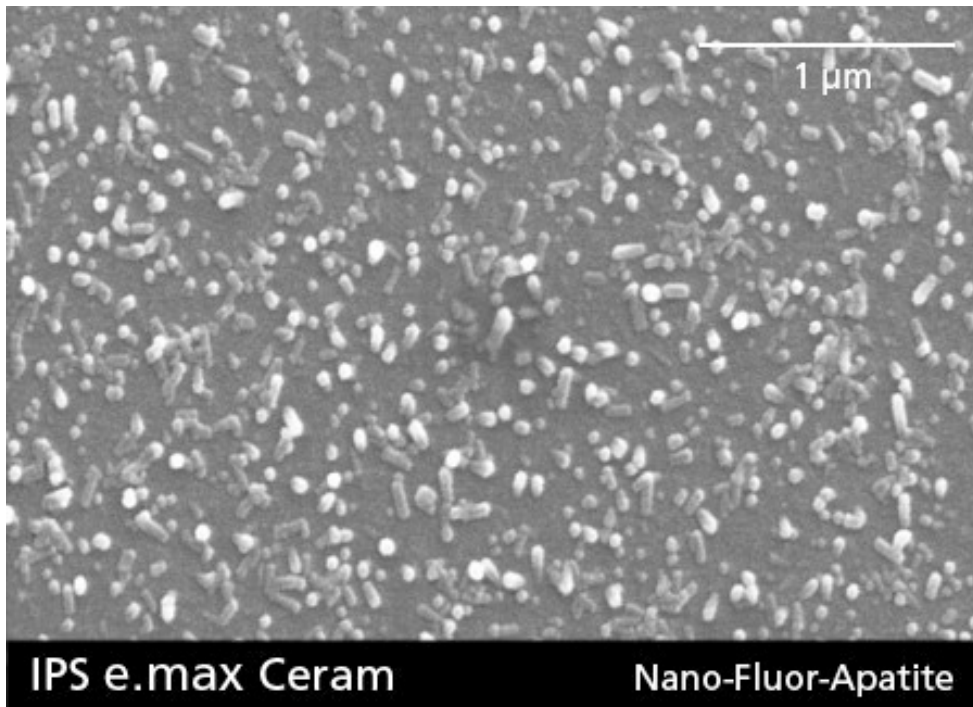


Figure 4-4. SEM image of polished and etched surface of e.max Ceram (EC) core ceramic showing the presence of needle-like nanofluorapatite crystals. Crystals are approximately 300 nm in length and 100 nm in diameter. [Image courtesy of Ivoclar Vivadent.]

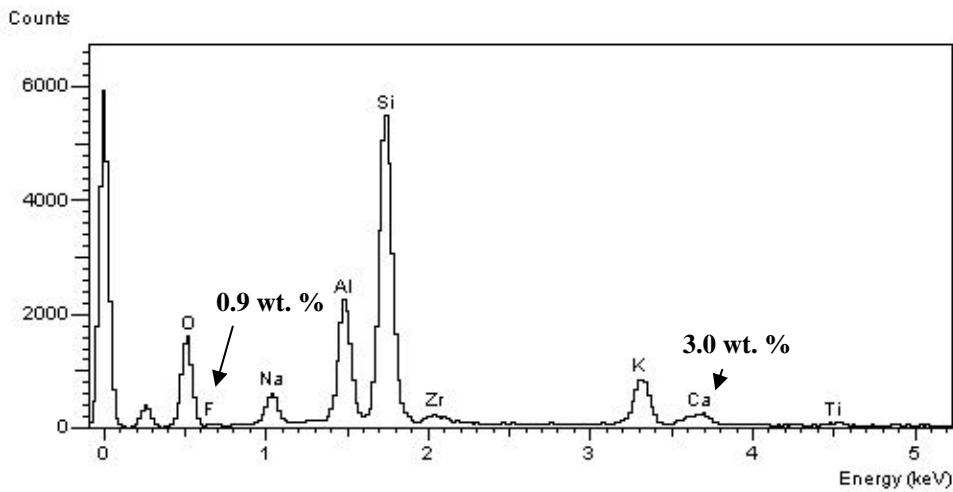


Figure 4-5. Energy dispersive X-ray spectroscopy (EDS) of e.max® Ceram (EV) veneer ceramic. Amount of Ca (~3 wt. %) present agrees with composition of veneer. Amount of F (~1 wt. %) present does not agree with composition of veneer.

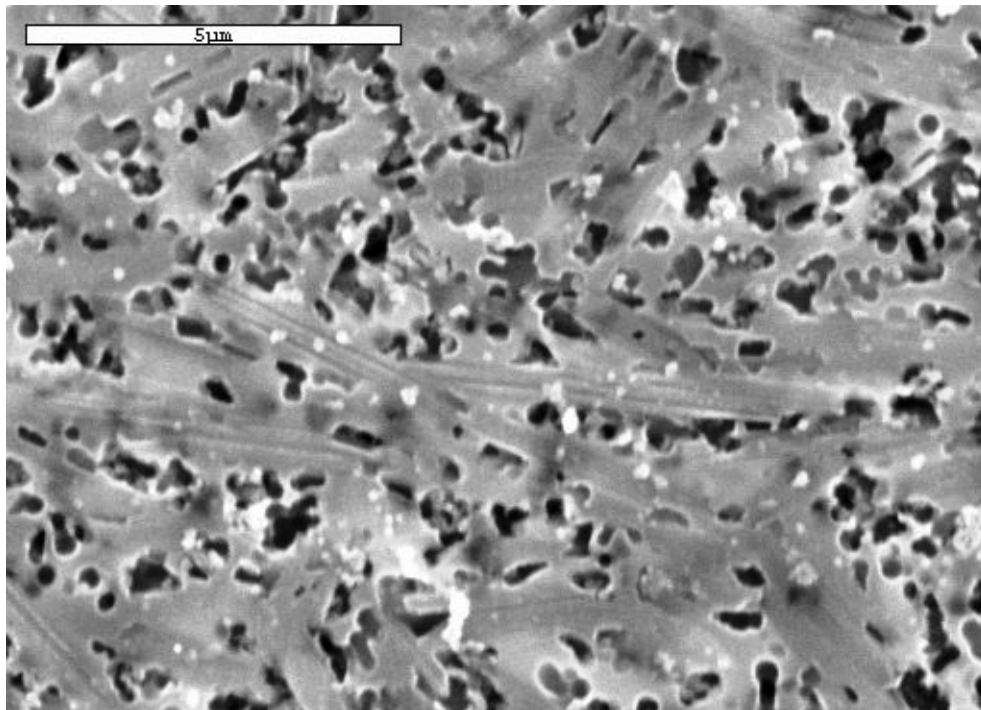


Figure 4-6. SEM micrograph of polished and etched surface e.max® Press (EC) core ceramic at a magnification of 10000x. Surface etched using 2.5 % HF solution, which did not provided enough contrast to measure the aspect ratio of the crystals.

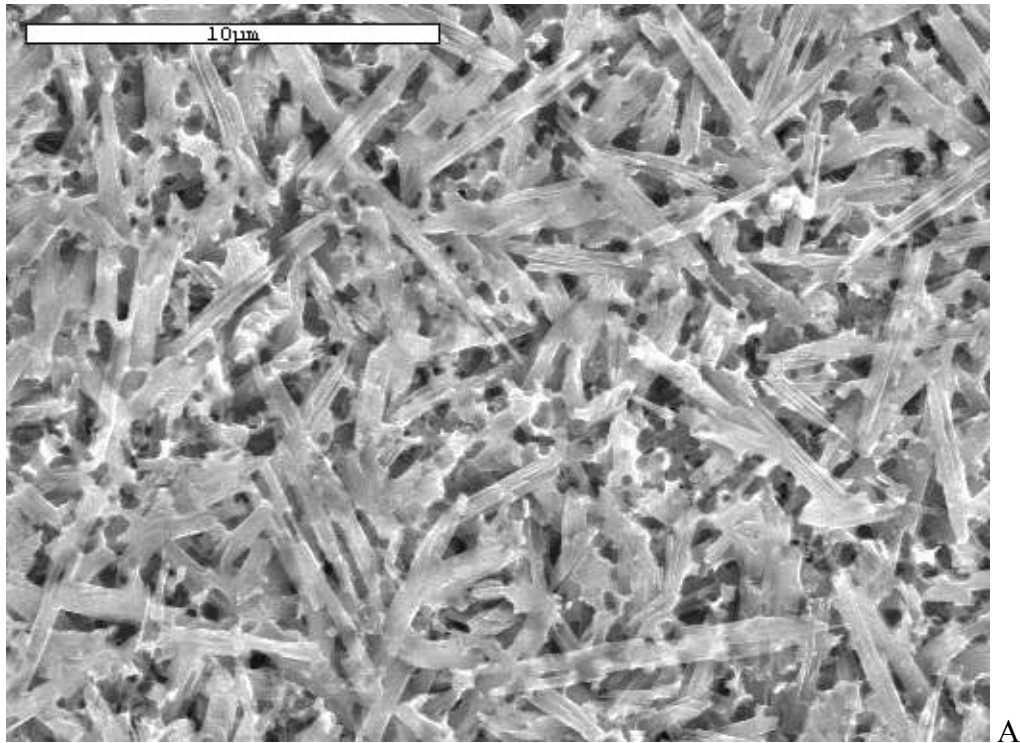
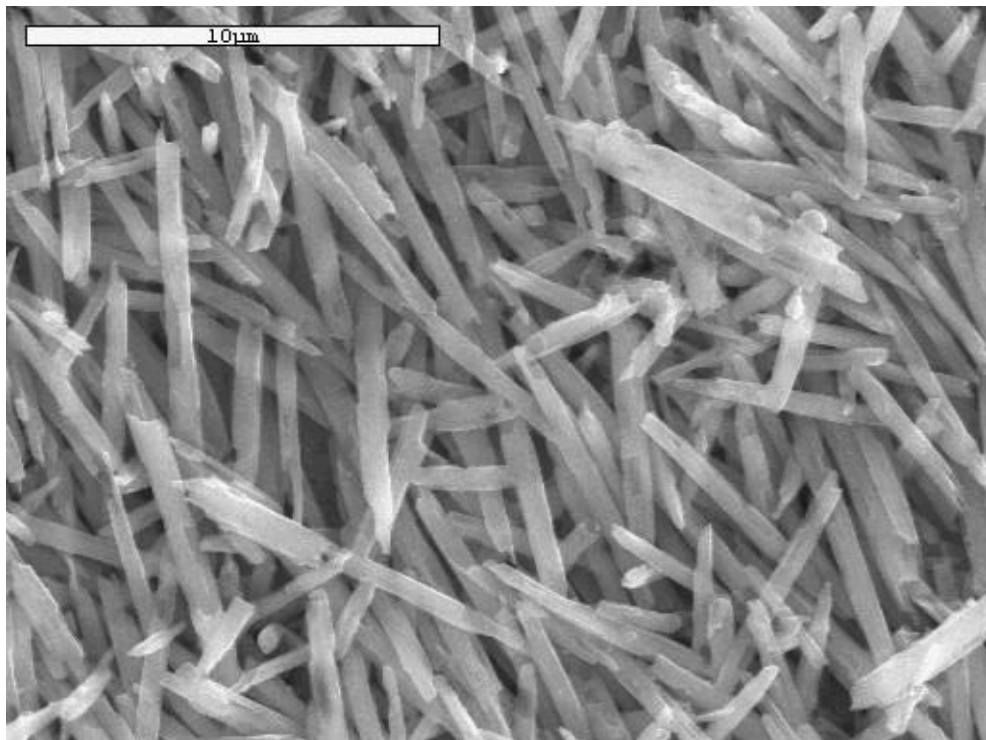


Figure 4-7. SEM micrograph of polished and etched surface e.max® Press (EC) core ceramic at a magnification of 5000x. A) Surface was etched using 2.5 % HF solution for 30s at room temperature and did not provide enough contrast to measure the aspect ration of the crystals. B) Surface etched using 30 % H<sub>2</sub>SO<sub>4</sub>/4 % HF solution for 10 s at room temperature. Etchant provided enough contrast to measure the aspect ratio of the lithium disilicate crystals.



B

Figure 4-7. Continued

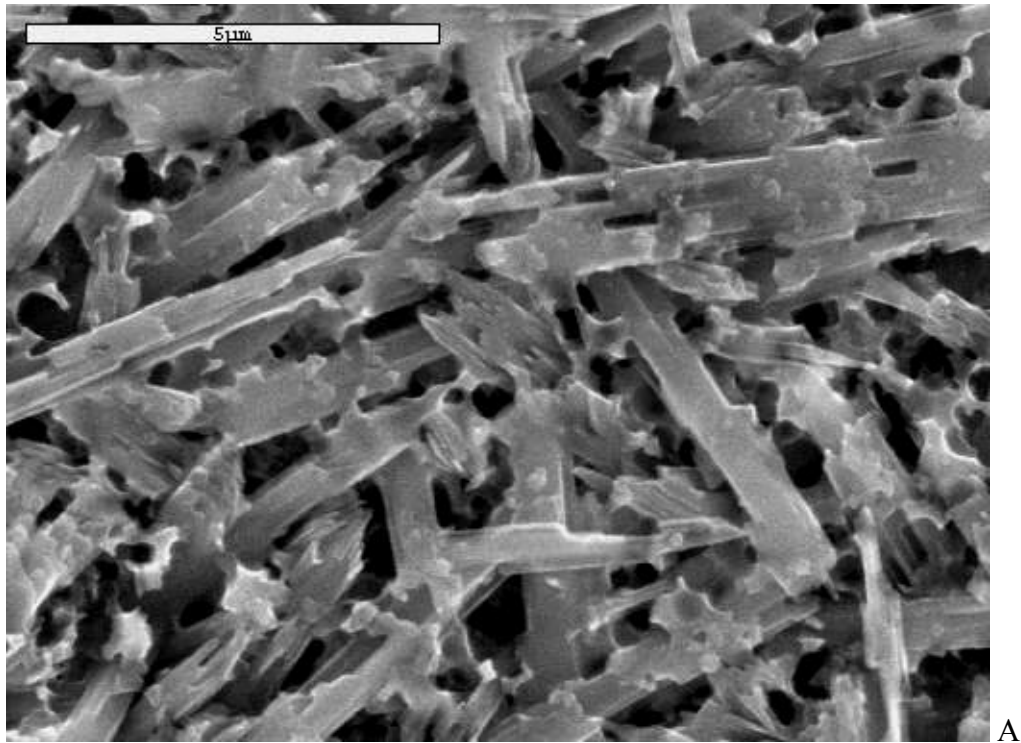


Figure 4-8. SEM micrograph of polished and etched surface e.max® Press (EC) core ceramic at a magnification of 10000x. A) Surface was etched using 2.5 % HF solution for 30s at room temperature and did not provide enough contrast to measure the aspect ration of the crystals. B) Surface etched using 30 % H<sub>2</sub>SO<sub>4</sub>/4 % HF solution for 10 s at room tempertaure. Etchant provided enough contrast to measure the aspect ratio of the lithium disilicate crystals.

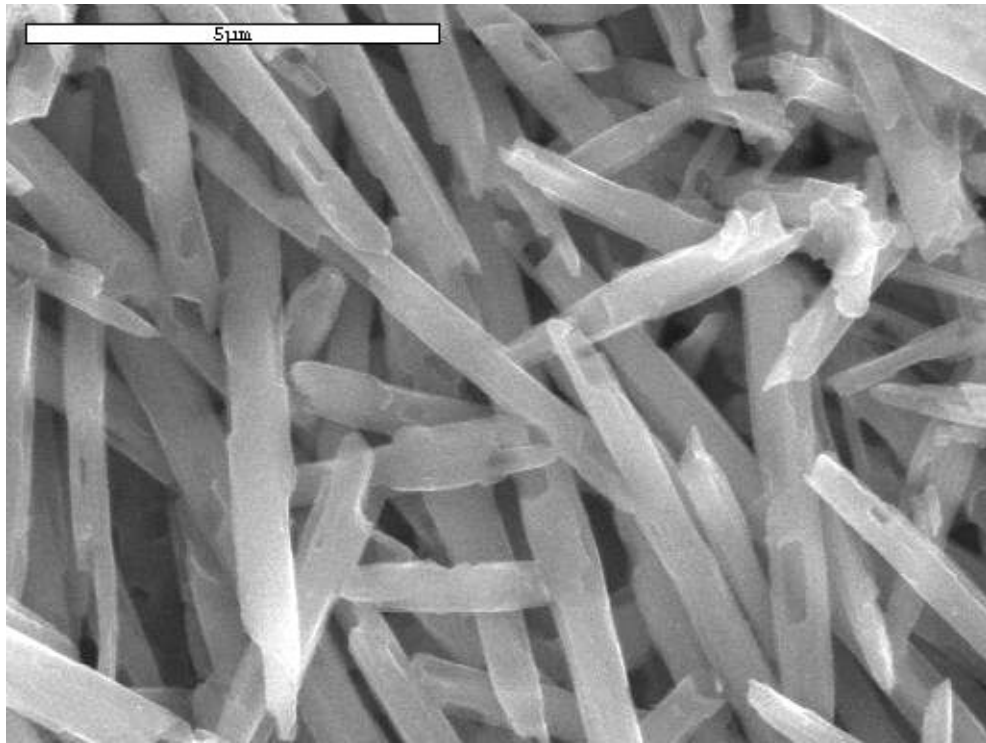


Figure 4-8. Continued

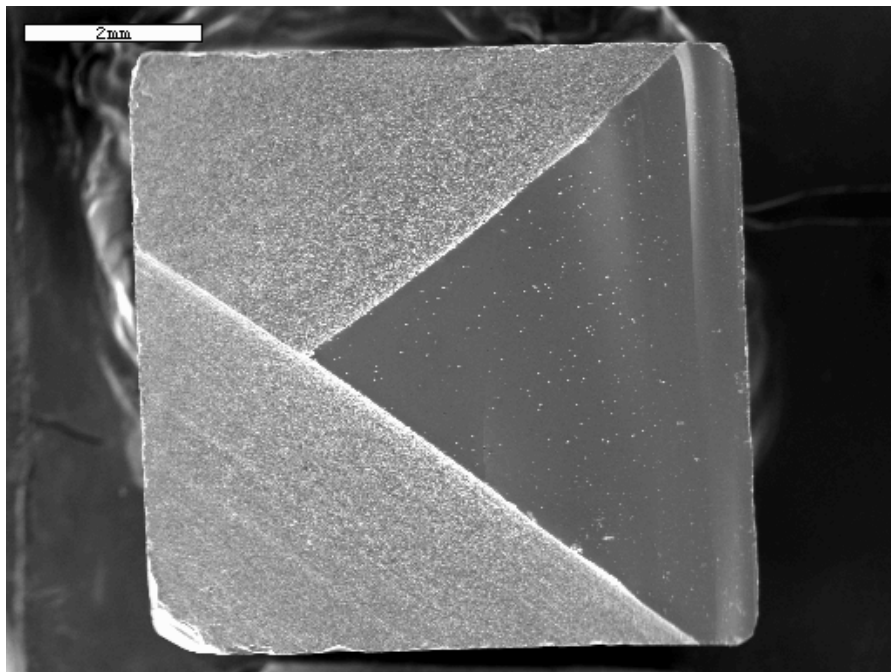


Figure 4-9. SEM image of fracture surface of chevron-notched soda-lime-silica flexure specimen showing that fracture surface is all mirror and no mist or hackle is present. [Image courtesy of Dr. Jia Hua Yan].

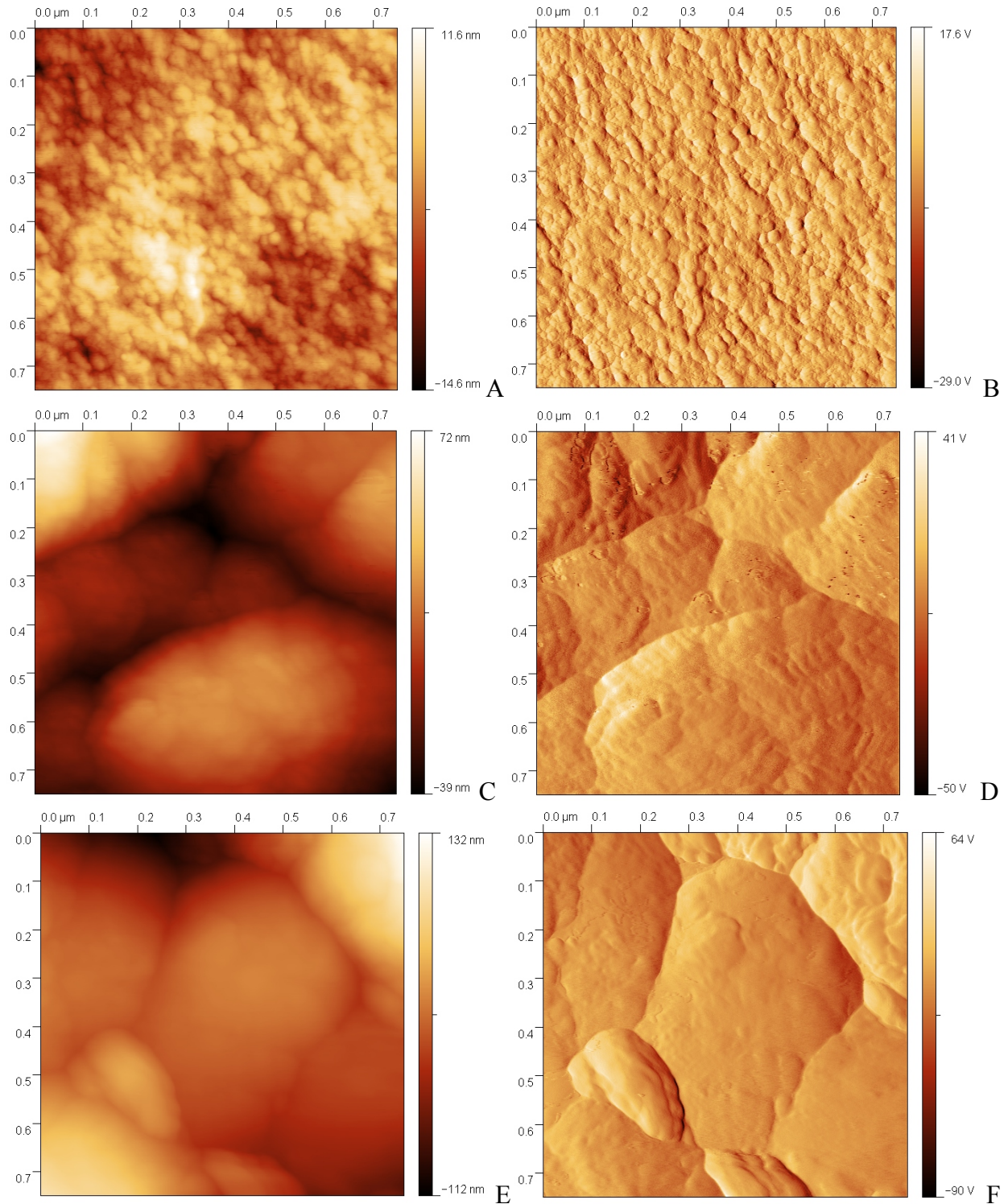


Figure 4-10. AFM height and amplitude scan image of soda-lime silica glass fracture surface at a scan area of  $(750 \text{ nm})^2$ . AFM images show that the roughness of the surface increases from the mirror region to the hackle region. A and B) Mirror region is rough on a nanometer scale. C and D) Mist region. E and F) Hackle region.

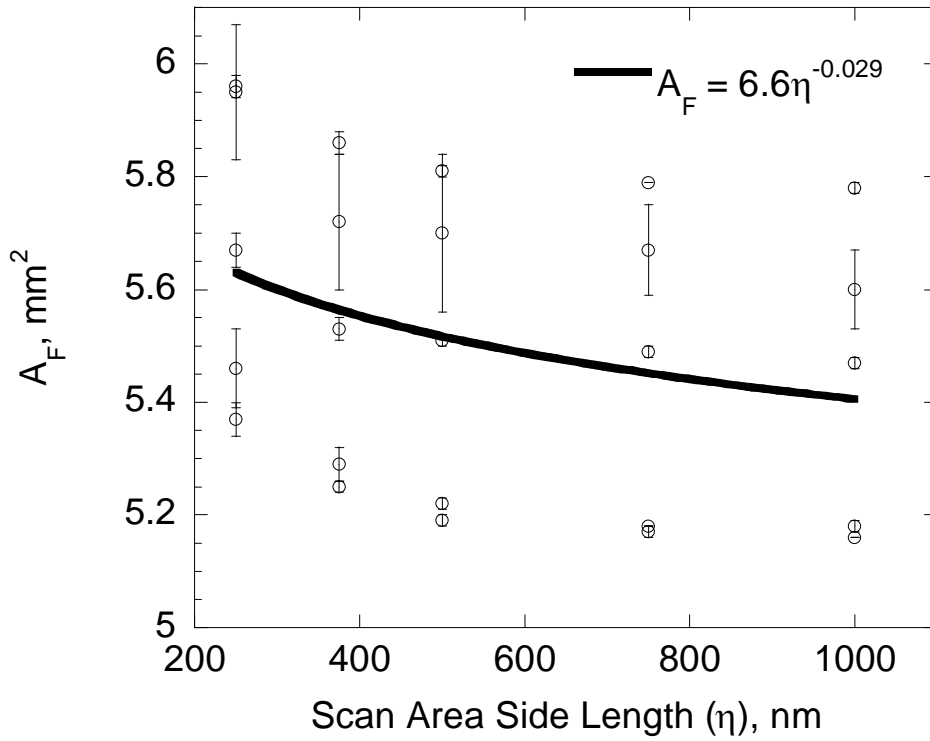


Figure 4-11. Fracture surface area ( $A_F$ ) as a function of scan area side length ( $\eta$ ) for chevron-notched soda-lime-silica bars.  $A_F$  is shown to increase confirming that  $A_F$  is greater than cross-sectional area. Circles represent average  $A_F$  from five scans at that particular scan area. Error bars represent standard deviation for  $A_F$  values.

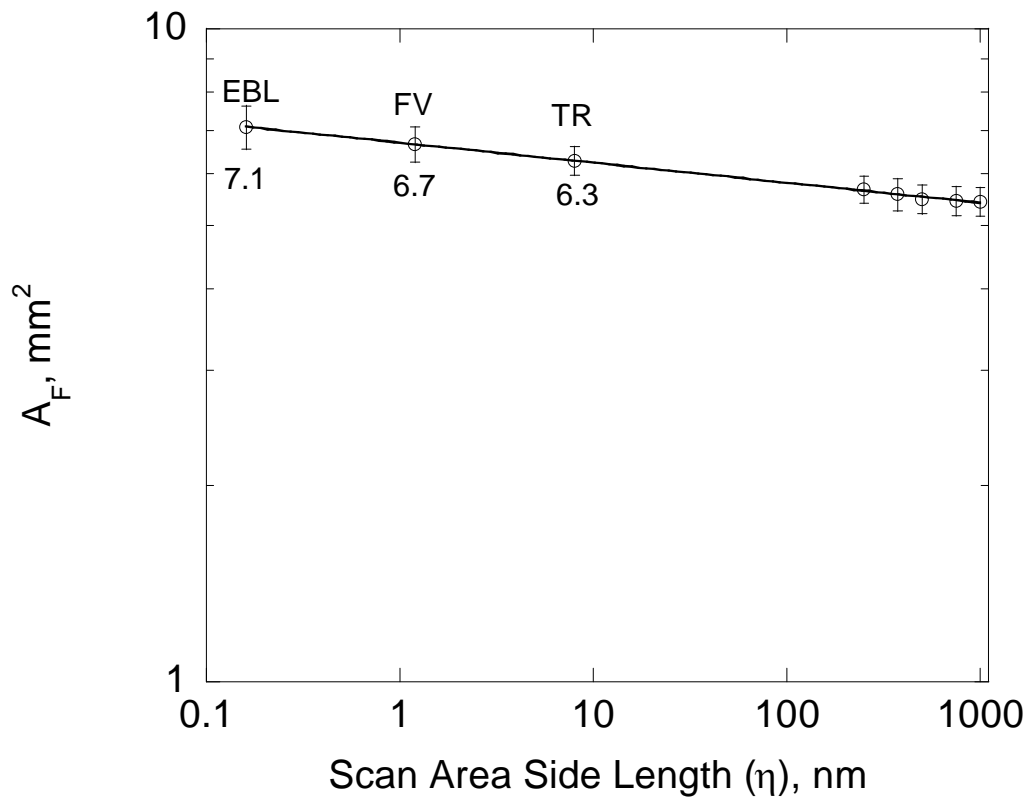


Figure 4-12. Projection of the average fracture surface area ( $A_F$ ) from the average  $A_F$  values for the chevron-notched (CN) specimens based on AFM data. Using the limits of the equilibrium bond length (EBL), free volume (FV), and tip radius (TR) result in an increase in the  $A_F$ , with EBL producing the largest  $A_F$  value. Circles represent average  $A_F$  of all the CN specimens. Error bars represent standard deviation for average  $A_F$  values.

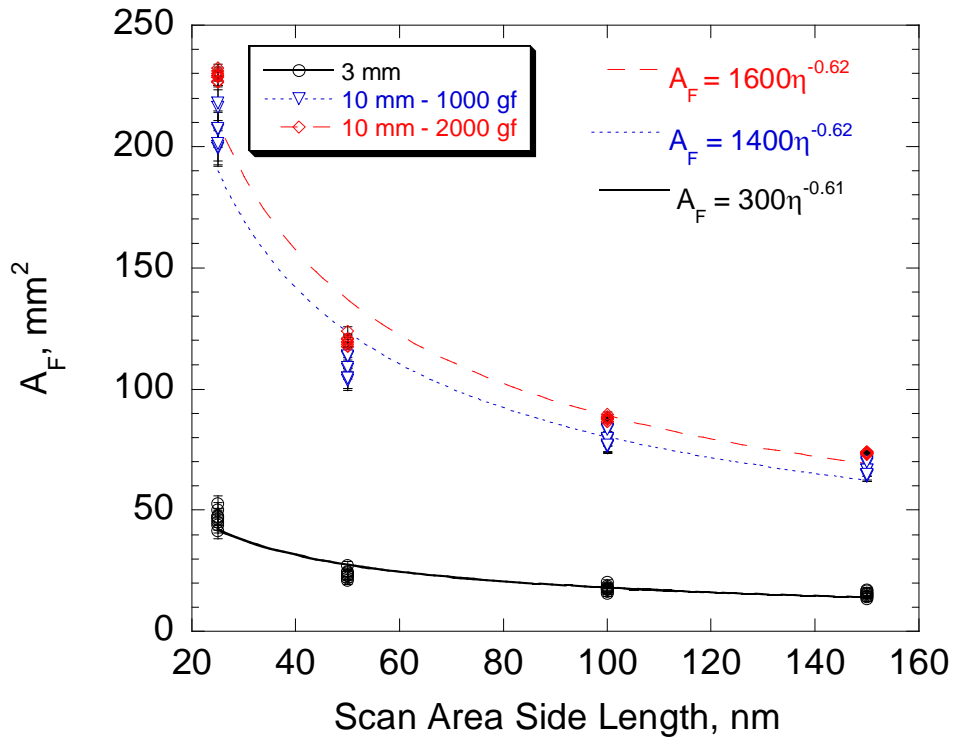


Figure 4-13. Fracture surface area ( $A_F$ ) as a function of scan area side length ( $\eta$ ).  $A_F$  is shown to increase confirming that  $A_F$  is greater than cross-sectional area. Data points represent average  $A_F$  each specimen in at a particular scan area. Error bars represent standard deviation for  $A_F$  values.

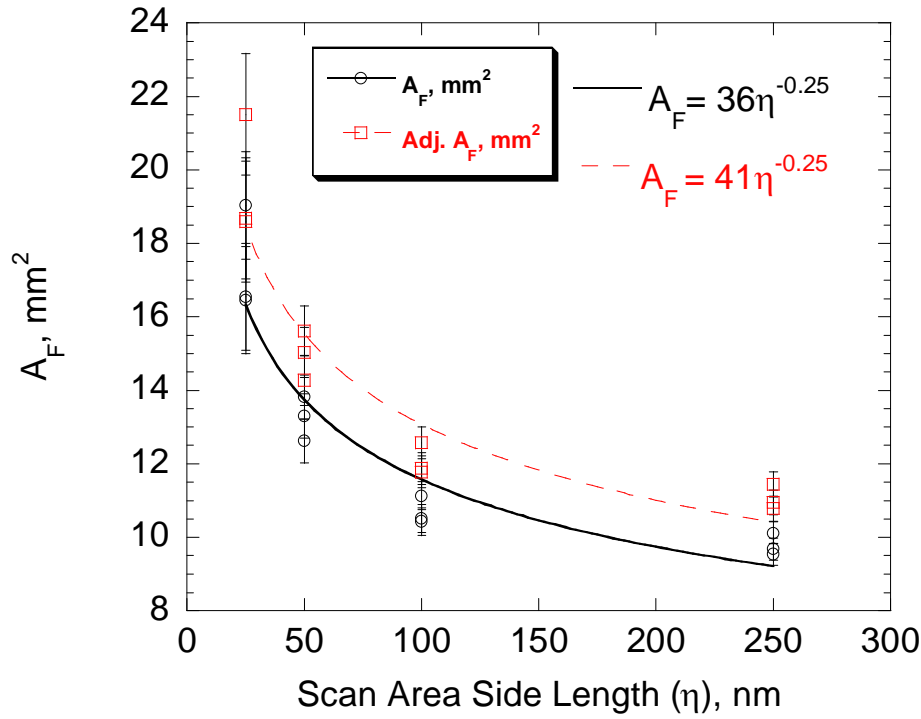


Figure 4-14. Fracture surface area ( $A_F$ ) and adjusted fracture surface area (Adj.  $A_F$ ) as a function of scan area side length ( $\eta$ ) for e.max® Ceram (EV) veneer bars. Adjusted surface are determined from optical profilometry. Data points represent average  $A_F$  each specimen in at a particular scan area. Error bars represent standard deviation for  $A_F$  values.

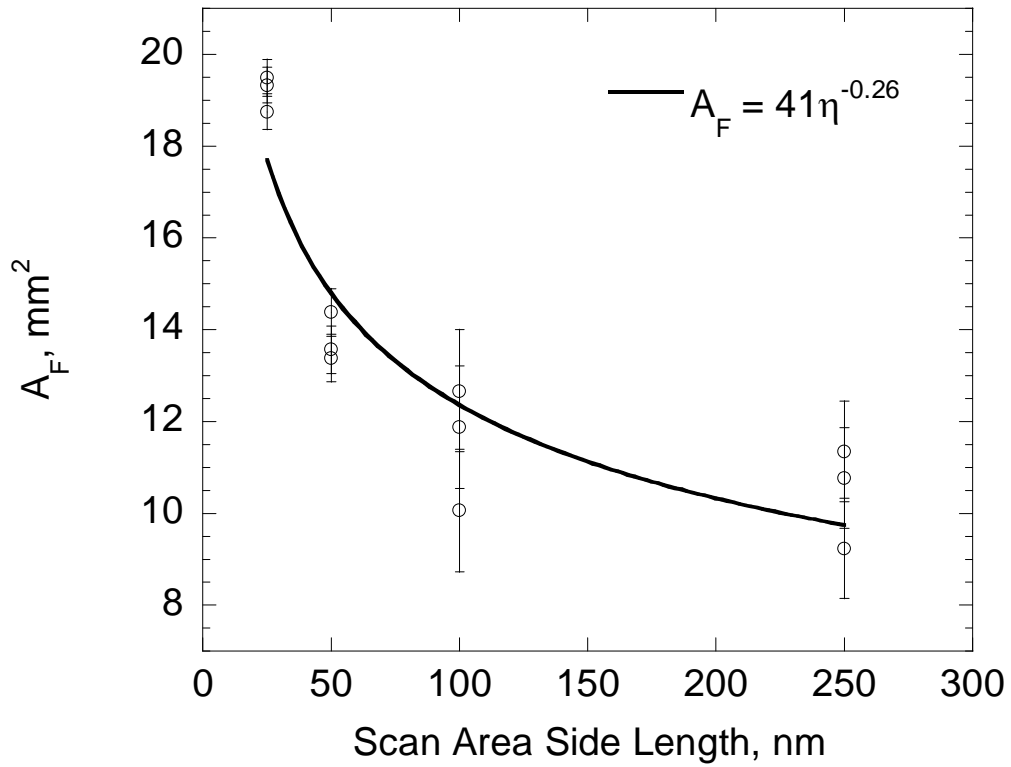


Figure 4-15. Fracture surface area ( $A_F$ ) as a function of scan area side length ( $\eta$ ) for e.max® Press (EC) core bars. Data points represent average  $A_F$  each specimen in at a particular scan area. Error bars represent standard deviation for  $A_F$  values.

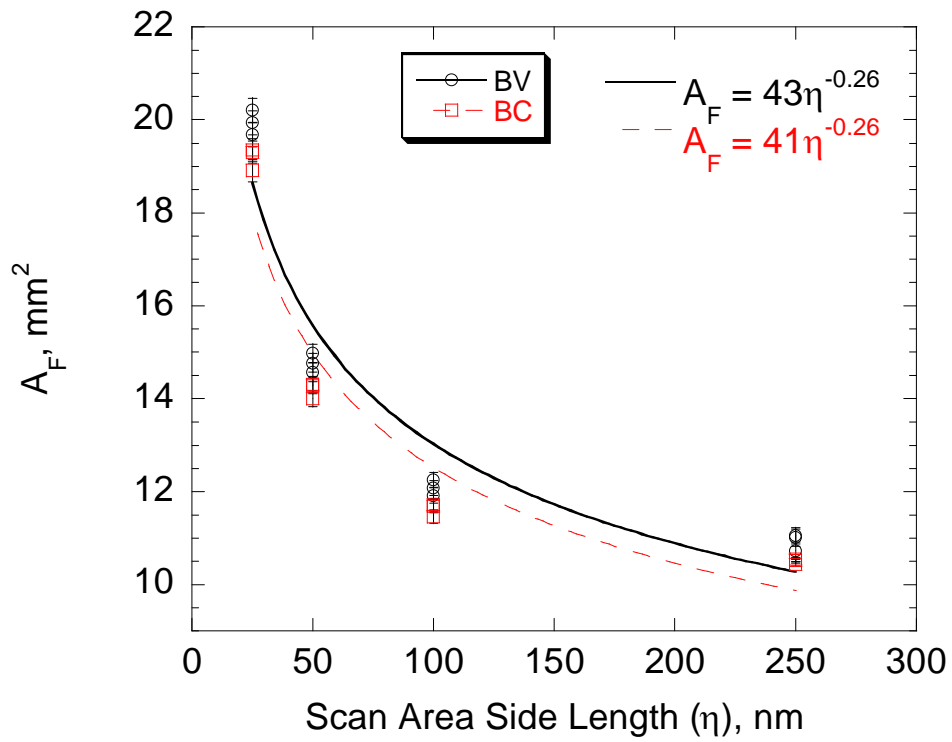


Figure 4-16. Fracture surface area ( $A_F$ ) as a function of scan area side length ( $\eta$ ) for veneer-indent (BV) and core-indent (BC) bilayers. Data points represent average  $A_F$  each specimen in at a particular scan area. Error bars represent standard deviation for  $A_F$  values.

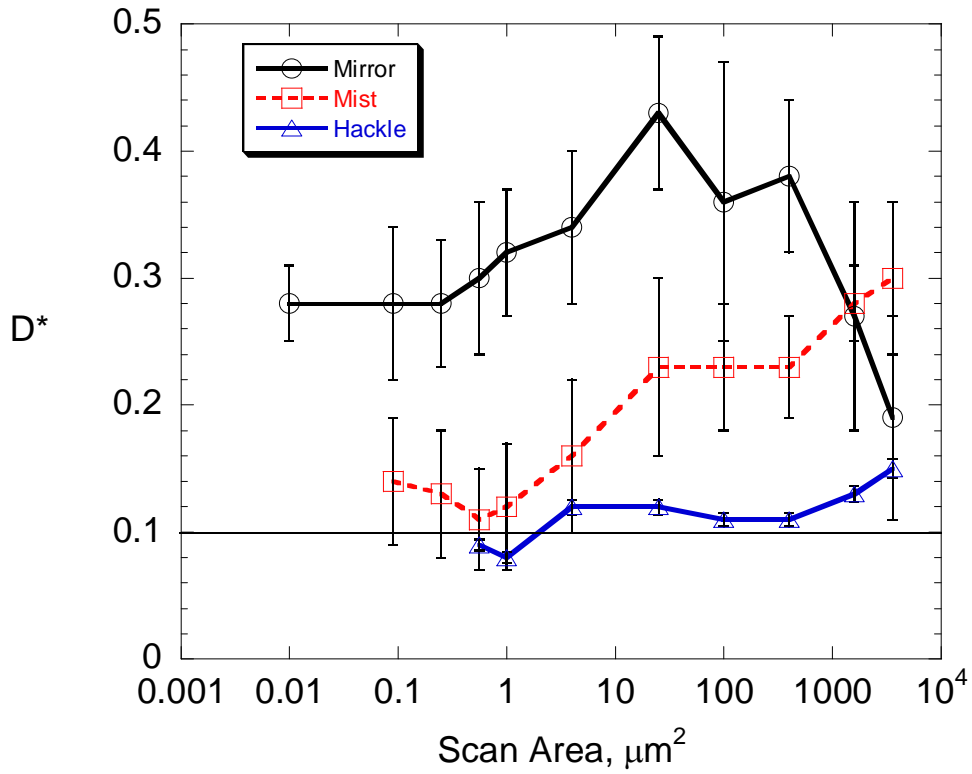


Figure 4-17. Fractal dimension increment ( $D^*$ ) of baria silica glass, plotted against scan area, determined from Gwyddion for mirror, mist, and hackle region. The horizontal line represents  $D^*$  of 0.1 determined from slit island method.

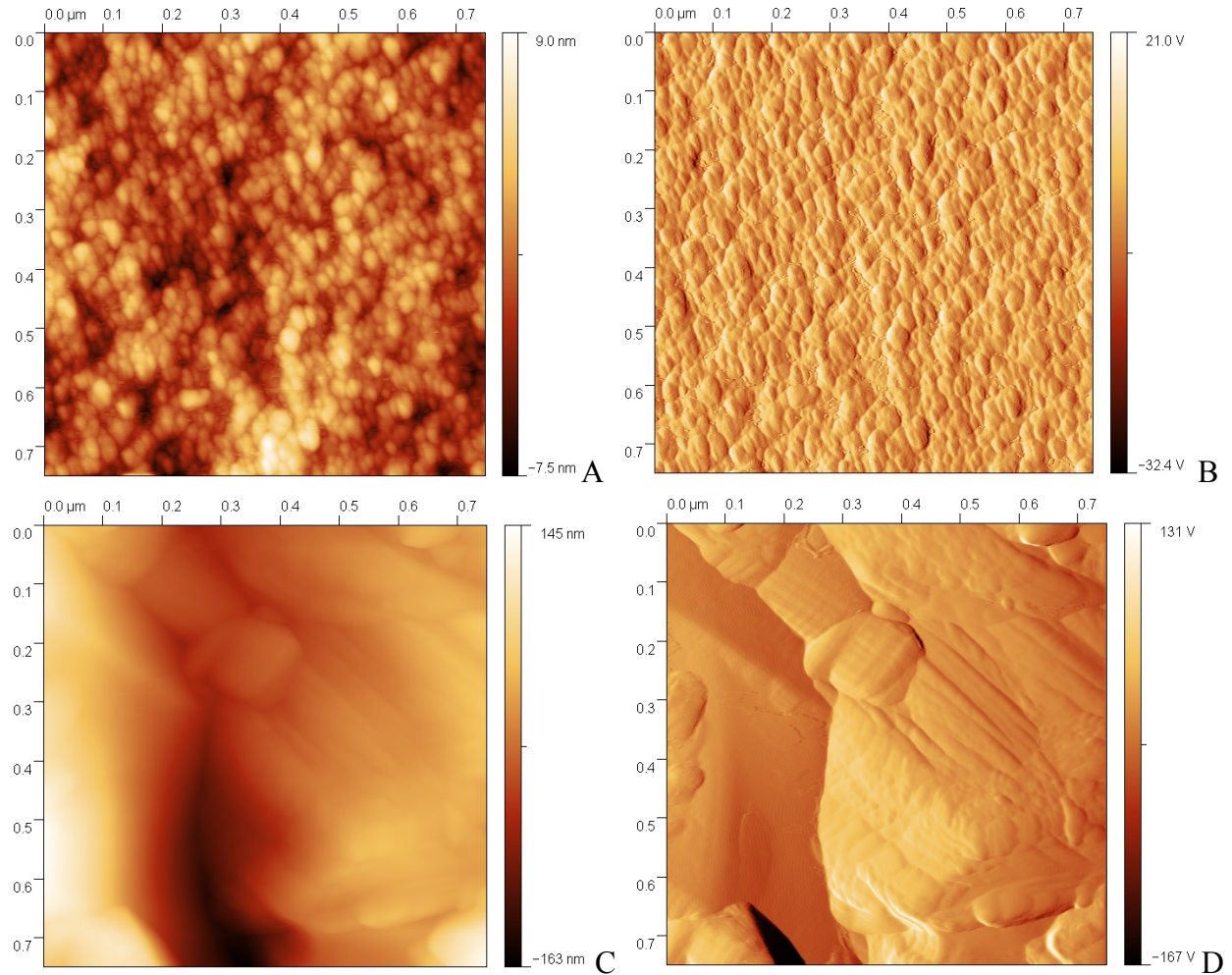


Figure 4-18. AFM scan image of e.max® Ceram (EV) veneer ceramic and e.max® Press (EC) core ceramic fracture surface at a scan area of  $(750 \text{ nm})^2$ . Color scale bar represents minimum and maximum heights in images. A and C are height images. B and D are amplitude images. Veneer has a fracture surface similar to soda-lime-silica. Core has a greater roughness than veneer at same scan area.

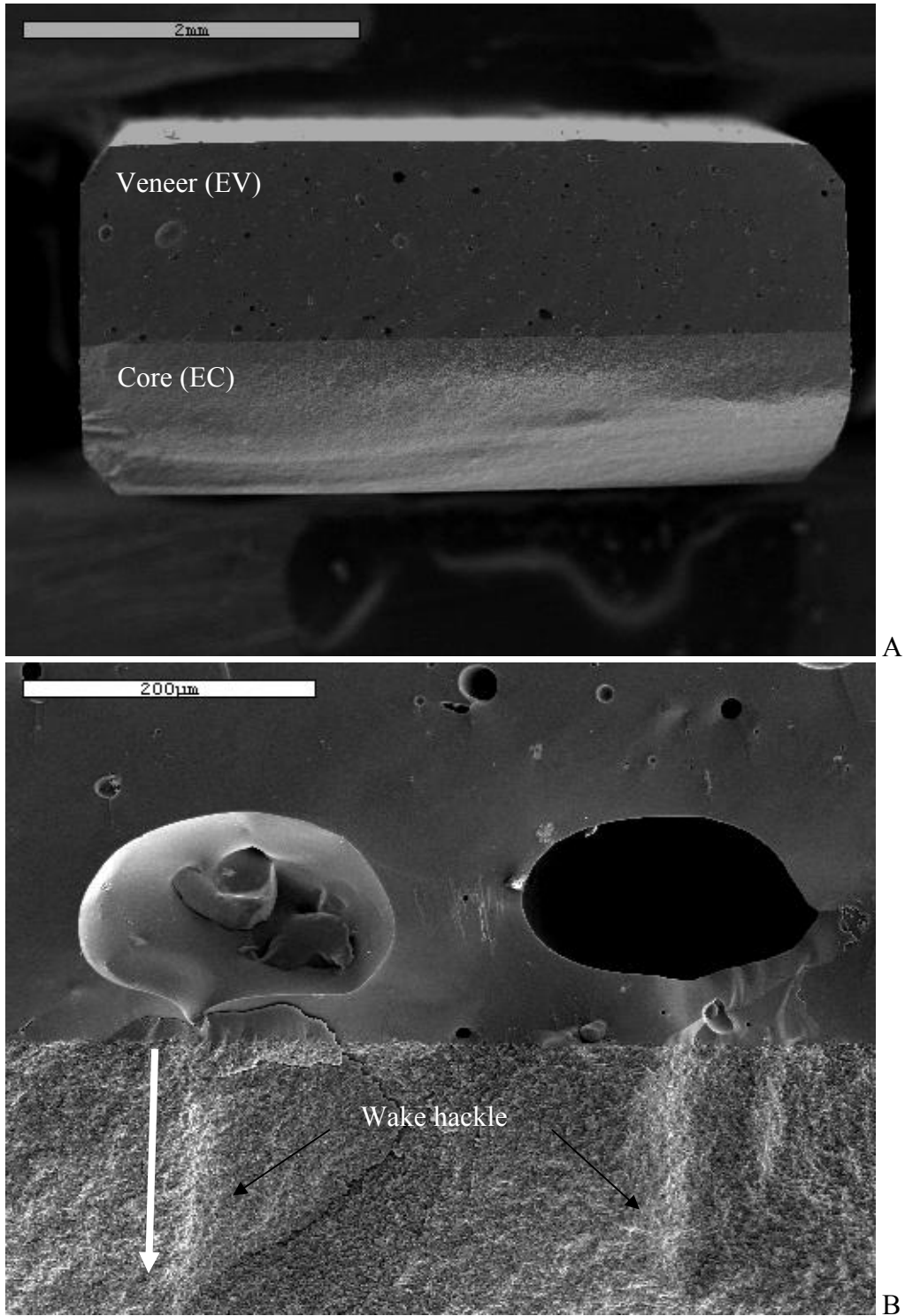


Figure 4-19. SEM images of veneer-indent bilayer (BV) fracture surface. A) Low magnification. B) Wake hackle marks traveling from pore in veneer into core show that fracture of bilayer was a continuous process. White arrow indicates crack direction.

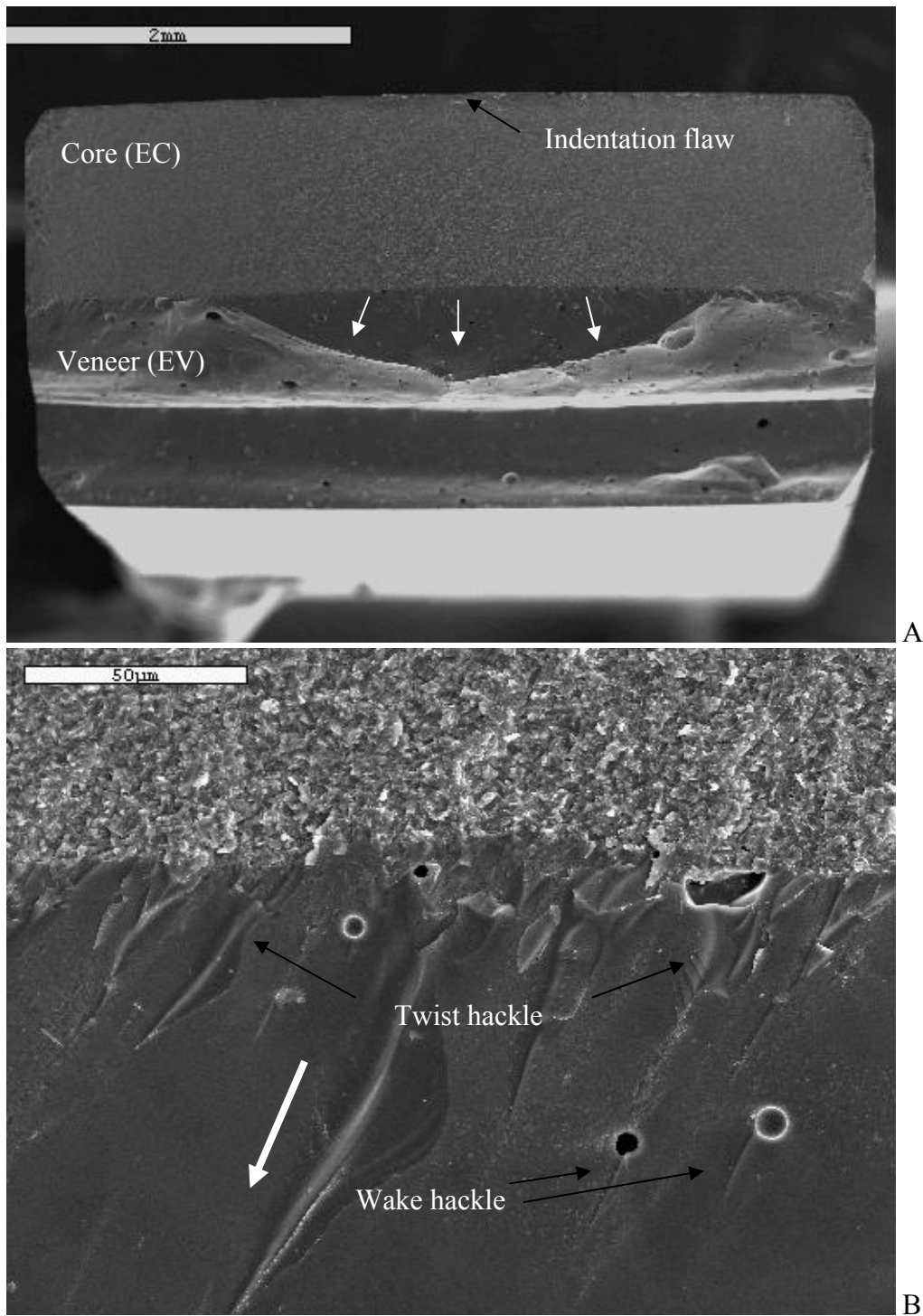


Figure 4.20. SEM images of core-indented bilayer (BC) fracture surface. A) Low magnification. B) Twist hackle marks indicate that fracture process was continuous. White arrows indicate crack direction.

## CHAPTER 5 CONCLUSIONS

The objectives of this project were to 1) test the hypothesis that the work of fracture method, using the actual fracture surface area, can be used to estimate the fracture energy of ceramic materials; 2) test the hypothesis that the work of fracture of a ceramic bilayer will be the same regardless of the location of crack initiation; and 3) test the hypothesis that the fractal dimension of the two materials in a bilayer will be the same regardless of the location of crack initiation.

The first hypothesis was shown to be true. For soda-lime-silica glass, the work of fracture method using the actual fracture surface area resulted in a decrease in the work of fracture when compared to using the cross-sectional area. The work of fracture, using the actual fracture surface area, was shown to be less than the fracture energy determined from traditional fracture mechanics tests and similar to the theoretical fracture energy for silica. The fracture energy determined from traditional fracture mechanics tests do not accurately measure the fracture energy generated during the fracture process because the fracture surface generated during fracture is not accounted for in these tests. This is the first time it has been experimentally demonstrated that the actual fracture surface area is critical to determining the minimum fracture energy. The work of fracture can be used to estimate the minimum fracture energy required to break the bonds in brittle materials. Therefore, the work of fracture can be used to determine the energy contributed in the creation of fracture surfaces in ceramics and will help engineers better understand the contributions to the total energy used to fracture a ceramic material.

The second hypothesis was shown to be false. The work of fracture values for the bilayer specimens were similar to those of the monoliths in which the crack was initiated. This

agreement implies that the work of fracture is dependent on the material in which the initial flaw that causes fracture is located in a bilayer structure. The core, which had a greater measured work of fracture than the veneer, resulted in a greater work of fracture in the core-indented bilayer when compared to the veneer-indented bilayer. Based on this information, the work of fracture should be used as another method in the mechanical characterization when determining the proper material for selecting and designing bilayer structures.

The third hypothesis was shown to be false. The fractal dimension of the veneer in the core-indented bilayer was not different from monolithic veneer. The fractal dimension of the core in the veneer-indented bilayer was not different from the monolithic core. This indicates that the fractal dimension of the materials in the bilayer did not change based on the site of crack initiation and propagation and that the fracture surface of the materials did not change when compared to monoliths of the same materials. Based on this information, the fractal dimension in each layer of the bilayer structure does not change due to the fracture process. Therefore, the fractal dimension is identified as being an intrinsic property of the fracture surface of the ceramic materials.

APPENDIX  
DETERMINATION OF THE HURST EXPONENT FOR SILICA GLASS

In this appendix, the Hurst exponent, a parameter that is used to define the fractal dimension for self-affine objects, i.e., ceramic fracture surfaces, is explained. Background on the Hurst exponent value for silica glasses is explored and the Hurst exponent is determined for the mirror region of soda-lime-silica glass.

**Background on the Hurst Exponent**

Mandelbrot and Passoja determined that fracture surfaces are fractal [40]. A fractal object can be either self-similar or self-affine. A self-similar surface is isotropic in magnification, i.e., in a three-dimensional Cartesian coordinate system,  $x, y, z \rightarrow \lambda x, \lambda y, \lambda z$  where  $\lambda$  is a scalar. A self-affine surface is anisotropic, i.e.,  $x, y, z \rightarrow \lambda x, \lambda y, \lambda^\zeta z$  where  $\zeta$  is called the Hurst exponent [73]. The Hurst exponent is also known as the Hurst dimension, the roughness exponent, or the roughness index. Since the fracture surface of ceramics scale differently out-of-plane compared to in-plane, ceramics are self-affine. For these ceramic fracture surfaces, there is a characteristic length at which the self-affinity of a surface can be measured. This length is called the correlation length ( $\xi$ ). For lengths greater than  $\xi$ ,  $\zeta$  approaches 1. For silica glass,  $\xi$  is inversely proportional to crack velocity, i.e.,  $\xi$  decreases from 80 to 30 nm for crack velocities from  $10^{-10}$  to  $10^{-4}$  m/s [74].

The Hurst exponent, like the fractal dimensional increment ( $D^*$ ), is bound by the values 0 and 1, where a  $\zeta$  value of 1 and a  $D^*$  value of 0 corresponds to a flat surface or line. The Hurst exponent is related to the fractal dimension ( $D$ ), but this relationship depends on the way  $D$  is defined [75]. If a curve or profile is covered with boxes ( $b$ ) of width  $\Delta x$  and height  $\Delta y$ , then the box dimension ( $D'$ ) is determined from the expression:

$$N(b; \Delta x; \Delta y) \propto b^{-D'} \tag{A-1}$$

where  $N(b; \Delta x; \Delta y)$  is the number of boxes used to cover the curve.  $D'$  is related to  $\zeta$  by the equation:

$$D' = 2 - \zeta \quad (\text{A-2})$$

If the same curve or profile is measured using a ruler length ( $\delta$ ) to measure the length of the curve  $L$ , then the divider dimension ( $D_d$ ) [76] is determined from the expression:

$$L \propto \delta^{1-D_d} \quad (\text{A-3})$$

where  $D_d$  is related to  $\zeta$  by the equation:

$$D_d = 1/\zeta \quad (\text{A-4}).$$

The Hurst exponent determined by  $D_d$  is bound from 0.5 to 1. Because of this difference in the way the fractal dimension is defined, it is better to use the Hurst exponent when describing self-affine objects to avoid any confusion.

### **Measurement Methods for Determining Hurst Exponent**

There are three methods that are used to measure  $\zeta$  of fracture surfaces: perpendicular sectioning, slit island, and direct surface area [75]. The perpendicular sectioning method measures  $\zeta$  from the profile of the fracture surfaces. The most used form of the perpendicular sectioning method is the profile length method. The profile length method, measures the length of a profile using different ruler length and is expressed in the equation

$$L = L_0 \delta^{1-D_d} \quad (\text{A-5})$$

where  $L_0$  is the projected length of the profile. The Hurst exponent is determined using Equation A-4.

The slit island method, discussed in Chapter 2, measures  $D$  from the contour of the fracture surface. The contours of the fracture surface, or islands, are used to measure the fracture

surface in two ways. The first way uses the perimeter (P) of the islands and determines the fractal dimension using the expression:

$$P \propto \delta^{1-D_d} \quad (\text{A-6})$$

which is similar to the perpendicular section method. The Hurst exponent from this method is calculated using Equation A-4. The second way the fractal dimension is measured is by determining the area (A) of the island in comparison to the perimeter. The fractal dimension measured in this way is expressed as

$$A \propto P^{2/D_d} \quad (\text{A-7})$$

The Hurst exponent measured using this method is calculated using Equation A-2. The problem with the slit island method is that since the contour of the fracture surface is used to determine D, then the self-similarity of the surface is measured instead of its self-affinity. Therefore, there is some debate as to whether the slit island method can be used to determine the Hurst exponent for self-similar materials.

The last method is the direct surface area measurement technique [77, 78]. This method is the profile method conducted in two-dimensions. The fracture surface area of a material is measured using a form of scanning probe microscopy (SPM) or scanning electron microscopy (SEM). The fractal dimension is determined from the equation

$$A = A_0 \delta^{2-D_d} \quad (\text{A-8})$$

where A is the fracture surface area,  $A_0$  is the cross-sectional area, and  $\delta$  is the side length of the SPM or SEM scan area. The Hurst exponent is calculated using the equation

$$\zeta = 1/(D_d - 1) \quad (\text{A-9})$$

which is similar to A-4 but  $D_d$  has a Euclidean dimension of 2 instead of 1.

## Hurst Exponent for Silica Glass

The Hurst exponent has been measured for silicate glasses, using some of the different methods mentioned previously, to determine if there is universality among all fractured materials in the Hurst exponent. Atomic force microscopy (AFM) was used in all of the measurements. The use of AFM has helped researchers achieve an improved view of the fracture surface and the ability to measure the fractal properties of fracture surfaces at small (nanometer) length scales.

Danguir et al. [79] measured  $\zeta$  for soda-lime-silica (SLS) glass. The mirror region was examined for crack velocities ranging from  $10^{-9}$  to  $10^{-7}$  m/s. Ten AFM height profiles of lengths of  $1.5 \mu\text{m}$  were taken perpendicular and parallel to the crack direction. The Hurst exponent was calculated based on the expression:

$$Z_{\max}(r) = r^{\zeta} \quad (\text{A-10})$$

where  $r$  is the width of the window used to measure the profiles and  $Z_{\max}(r)$  is the difference between the maximum and minimum heights within the width of the window. It was shown that there were two different values for  $\zeta$  determined by a crossover length ( $\xi_C$ ). For large length scales ( $r > \xi_C$ ),  $\zeta = 0.78$  and for small length scales ( $r < \xi_C$ )  $\zeta = 0.5$ . The direction of the profile was shown to have no significant effect on  $\zeta$ . This worked confirmed that the Hurst exponent is affected by the length scale used to determine it.

Bonamy et al. [74] measured  $\zeta$  for a silica glass. The fracture surface was generated at crack velocities of  $10^{-11}$  to  $10^{-4}$  m/s. The fracture surface was scanned using an AFM at a scan area of  $(1 \mu\text{m})^2$ . A one-dimension height-height correlation function ( $G(x)$ ):

$$G(x) = \lim_{L \rightarrow \infty} \frac{1}{L} \int_0^L [h(x'+x) - h(x')]^2 dx' \quad (\text{A-11})$$

where  $L$  is the section length,  $h(x')$  is the height of the surface at point  $x'$ , and  $h(x'+x)$  is the height at a distance  $x$  away from point  $x'$ , was used to determine the fractal dimension based on the expression:

$$G(x) \propto x^{4-2D'} \quad (\text{A-12})$$

Using Equation A-12 and A-2,  $\zeta = 0.75$  for  $\zeta \leq 80$  nm. This value agrees with the value obtained by Danguir et al. at large length scales.

Wiederhorn et al. [70] measured  $\zeta$  for SLS glass based on the roughness of the fracture surface. The mirror region of SLS glass was measured at velocities ranging from  $10^{-10}$  to 10 m/s for AFM scan areas of  $(0.5\mu\text{m})^2$  to  $(5\mu\text{m})^2$ . The Hurst exponent was determined from the equation

$$R_q = aL_0^\zeta \quad (\text{A-13})$$

where  $R_q$  is the root-mean-squared (RMS) roughness,  $L_0$  is the edge length of the AFM scan area, and  $a$  is a constant. It was shown that  $\zeta$  was inversely proportional to the crack velocity. The Hurst exponent ranged from 0.18 for a crack velocity of 10 m/s to 0.28 for  $10^{-10}$  m/s.

The Hurst exponent values reported by Wiederhorn et al. were less than the values reported by Bonamy et al. and Danguir et al. It is possible that  $\zeta$  values measured by Wiederhorn et al. are the  $D^*$  values for SLS glass. Based on the  $D^*$  values in Table 4-5, this assumption appears to be correct. Based on the lesser  $\zeta$  values reported, Wiederhorn et al. showed that this difference is due to the method used to determine the RMS roughness. The Hurst exponent was measured for section lengths of 2 and 5  $\mu\text{m}$ . When measuring the line profiles of the fracture surface from AFM scans,  $\zeta$  is determined from the expression

$$\omega \propto L_0^\zeta \quad (\text{A-14})$$

where  $\omega$  is the RMS roughness for a line and  $L_0$  is the length used to measure the line. Using this method,  $\zeta = 0.75$  for 2  $\mu\text{m}$  and 0.78 for 5  $\mu\text{m}$ . When the area of the fracture surface is used to determine roughness,  $\zeta$  was 0.92 for 2  $\mu\text{m}$  and 0.95 for 5  $\mu\text{m}$ . This showed that measuring  $\zeta$  based on one-dimensional (line profiles) and two-dimensional (surface areas) does not result in the same value and that Equations A-13 and A-14 are not equivalent. Measuring  $\zeta$  based on area roughness is not an accurate method.

As mentioned in Chapter 3, the fracture surface area of chevron-notched SLS glass was measured using the AFM. The fracture surface of the chevron-notched specimen was all mirror. Using the direct surface area measurement method, the fracture surface was measured at scan areas from  $(1 \mu\text{m})^2$  to  $(250 \text{ nm})^2$ . Using Equations A-8 and A-9,  $\zeta = 0.97$ . This value is similar to that reported by Wiederhorn et al. when using the scan area to determine  $\zeta$  but greater than the values reported by Danguir et al. and Bonamy et al. This difference, as reported by Wiederhorn et al., is due to the larger length scale, 100 to 1000 nanometers as opposed to tens of nanometers, used in determining  $\zeta$  and determining  $\zeta$  based on two-dimensional measurements.

From Chapter 4, the fractal dimension of SLS glass was measured using AFM and the Gwyddion software. From Table 4-5,  $D$  for the mirror region was 2.26 using cube counting and 2.29 using triangulation. For cube counting, the slope of the number of cubes versus the box length is  $D'$ . For triangulation, the slope of the surface area versus the side length of the triangle is two minus  $D_d$ . Therefore,  $\zeta = 0.74$  for cube counting and 0.78 for triangulation. These values are similar to the values reported by Danguir et al. and Bonamy et al. This showed that data acquired from two-dimensional measurements could be used to measure  $\zeta$ .

As Table A-1 shows,  $\zeta$  for SLS and silica glass is dependent on the measurement technique used and the length scale used to determine  $\zeta$ . For length scales greater than the

crossover or critical length for the material,  $\zeta \approx 0.75$ . For lengths less than this critical length,  $\zeta = 0.5$ . Measurement of  $\zeta$  at larger length scales, on the order of hundreds or thousands of nanometers, results in  $\zeta$  approaching 1. Therefore, the length scale used and the measurement method must be taken into account when measuring  $\zeta$  for glasses.

Table A-1. Hurst exponent for mirror region of silicate glasses from different experimental methods.

Experiment	Hurst exponent
Danguir et al.	0.5; 0.78
Bonamy et al.	0.75
Wiederhorn et al.	
Initial area roughness	0.18-0.28
Line roughness	0.75 (2 $\mu\text{m}$ ); 0.78 (5 $\mu\text{m}$ )
Area roughness	0.92 (2 $\mu\text{m}$ ); 0.95 (5 $\mu\text{m}$ )
Direct surface area (Smith)	0.97
Triangulation (Smith)	0.78
Cube counting (Smith)	0.74

## LIST OF REFERENCES

1. Apel E, Deubener J, Bernard A et al (2008) *J Mech Behav Biomed Mater* 1:313
2. Höland W, Schweiger M, Frank M et al (2000) *J Biomed Mater Res* 53:297
3. Taskonak B (2004) University of Florida, Gainesville, FL
4. Taskonak B, Anusavice KJ, Mecholsky JJ (2004) *Dent Mater* 20:701
5. Thompson GA (2000) *Dent Mater* 16:235
6. Bühler-Zemp P, Völkel T (2005) Scientific Documentation IPS e max® Press:1
7. Pavon J, Jimenez-Pique E, Anglada A et al (2006) *Acta Mater* 56:3592
8. Cazzato A, Faber KT (1997) *J Am Ceram Soc* 80:181
9. Taskonak B, Yan JH, Mecholsky Jr. JJ et al (2008) *Dent Mater* 24:1077
10. Was GS, Jones JW, Kalnas CE et al (1994) *Surf Coat Technol* 65:77
11. Qasim T, Ford C, Bongue-Boma M et al (2006) *Mater Sci Engin A* 419:189
12. Atkinson A, Selçuk A (1999) *Acta Mater* 47:867
13. Clegg WJ, Kendall K, Alford NM et al (1990) *Nature* 347:455
14. Jung YG, Shin JH, Ha CG et al (2002) *Mater Lett* 56:1093
15. Lakshminarayanan R, Shetty DK, Culter RA (1996) *J Am Ceram Soc* 79:79
16. Höland W, Beall G (2002) *Glass-Ceramic Technology*. The American Ceramic Society, Westerville
17. McMillan PW (1979) *Glass-Ceramics*, 2nd edn. Academic Press, London
18. Kasakov NF (1985) In:Kazakov NF (ed) *Diffusion bonding of materials*, 1st edn. Pergamon Press Inc., New York
19. Dunkerton SB (1991) In:Stephenson DJ (ed) *Diffusion Bonding 2*, 1st edn. Elsevier Applied Science, London
20. Yen TF, Chang YH, Yu DL et al (1991) *Mater Sci Engin A* 147:121
21. Sakai M, Ichikawa H (1992) *Int J Fract* 55:65
22. Varin R (2001) *Scr Mater* 45:1357

23. Inagaki M, Urashima K, Toyomasu S et al (1985) *J Am Ceram Soc* 68:704
24. Tattersall HG, Tappin G (1966) *J Mater Sci* 1:296
25. Lucksanasombool P, Higgs WAJ, Higgs, R. J. E. D. et al (2001) *Biomater* 22:3127
26. Currey JD (1977) *Proc R Soc Lond B* 196:443
27. Neves NM, Mano JF (2005) *Mater Sci Eng C* 25:113
28. Rogers LL, Moyle DD (1988) *J Biomech* 21:919
29. Bazant ZP (1996) *J Eng Mech-ASCE* 122:138
30. Davidge RW, Tappin G (1968) *J Mater Sci* 3:165
31. Bueno S, Baudin C (2009) *Composites Part A* 40:137
32. Bermejo R, Torres Y, Sánchez-Herencia AJ et al (2006) *Acta Mater* 54:4745
33. Behr M, Rosentritt M, Faltermeier A et al (2005) *Dent Mater* 21:804
34. Nakayama J (1965) *J Am Ceram Soc* 48:583
35. Eick JD, Kotha SP, Chappelow CC et al (2007) *Dent Mater* 23:1011
36. Turell MB, Bellare A (2004) *Biomater* 25:3389
37. Wong WLE, Gupta M (2007) *Composites Sci Technol* 67:1541
38. Kulawansa DM, Jensen LC, Langford SC et al (1994) *J Mater Res* 9:476
39. Hill TJ, Della Bona JJ, Mecholsky JJ (2001) *J Mater Sci*:2651
40. Mandelbrot BB, Passoja DE, Paullay AJ (1984) *Nature* 308:721
41. Fractal dimension of broccoli. (2002) *The Physics Factbook*, New York.  
<http://hypertextbook.com/facts/2002/broccoli.shtml>. Accessed March/10 2009
42. Tanaka M, Kayama A, Sato Y et al (1998) *J Mater Sci Lett*:1715
43. Mecholsky JJ, Passoja DE, Feinberg-Ringel KS (1989) *J Am Ceram Soc* 72:60
44. West J, Mecholsky J, Hench L (1999) *J Non Cryst Solids* 260:99
45. Xie HP, Wang JA, Stein E (1998) *Phys Lett A* 242:41
46. Santos SFD, Rodrigues JDA (2003) *Mater Res* 6:219
47. Underwood EE, Banerji K (1986) *Mater Sci Eng* 80:1

48. Wang SG (2004) *Physica B* 348:183
49. Richardson LF (1961) *Gen Syst* 6:139
50. Chantikul P, Anstis GR, Lawn BR et al (1981) *J Am Ceram Soc* 64:539
51. Beer FP, Johnston ER (1992) *Mechanics of materials*, 2nd edn. McGraw-Hill, Inc., New York
52. Taskonak B, Mecholsky JJ, Anusavice KJ (2004) *Biomater* 26:3235
53. Lawn B (1993) *Fracture of brittle solids*, 2nd edn. Cambridge University Press, Cambridge, UK
54. Mecholsky JJ (2001) In: Buschow KH, Cahn RW, Flemings MC et al (eds) *Encyclopedia of materials: science and technology*, 1st edn. Elsevier Science Ltd., St. Louis
55. ASTM International (1999) C 1421-99:641
56. Gwyddion - Free SPM(AFM,SNOM/NSOM, STM, MFM, ...) data analysis software. (2008) Czech Metrology Institute, Brno. <http://gwyddion.net>. Accessed December 01 2008
57. Douketis C, Wang Z, Haslett TM et al (1995) *Phys Rev B* 51:11024
58. Zösch A, Zahn W (1997) *Fresenius J Anal Chem* 358:119
59. Mannelquist A, Almqvist N, Fredriksson S (1998) *Appl Phys A* 66:S891
60. Horcas I, Fernández R, Gómez-Rodríguez JM et al (2007) *Rev Sci Instrum* 78:013705
61. Hill TJ (1998) University of Florida, Gainesville
62. Höland W, Rheinberger V, Frank M (1999) *J Non-Cryst Solids* 253:170
63. Tsalouchou E, Cattell M, J., Knowles J, C. et al (2008) *Dent Mater* 24:308
64. Soboyejo WO (2003) *Mechanical properties of engineered materials*, 1st edn. CRC Press, Princeton, NJ
65. Charles RJ (1961) In: Burke JE (ed) *Progress in Ceramic Science*, 1st edn. Pergamon Press, New York
66. Swiler TP, Varghese T, Simmons JH (1995) *J Non-Cryst Solids* 181:238
67. Mecholsky JJ, Rice RW, Freiman SW (1974) *J Am Ceram Soc* 57:440
68. Mecholsky JJ, Plaia JR (1992) *J Non-Cryst Solids* 146:249

69. Thompson JY, Anusavice KJ, Balasubramaniam B et al (1995) *J Am Ceram Soc* 78:3045
70. Wiederhorn SM, Lopez-Cepero JM, Wallace J et al (2007) *J Non-Cryst Solids* 353:1582
71. Drummond JL, Thompson M, Super BJ (2005) *Dent Mater* 21:586
72. Naman A, Anusavice KJ, Mecholsky JJ (1994) *J Dent Res* 73:196
73. Mandelbrot BB (1982) *The Fractal Geometry of Nature*, 1st edn. Freeman, San Francisco
74. Bonamy D, Ponson L, Prades S et al (2006) *Phys Rev Lett* 97:135504
75. Milman VY, Stelmashenko NA, Blumenfeld R (1994) *Prog Mater Sci* 38:425
76. Feder J (1988) *Fractals*, 1st edn. Plenum, New York
77. Denley DR (1990) *Ultramicroscopy* 33:88
78. Friel JJ, Pande CS (1993) *J Mater Res* 8:100
79. Daguer P, Nghiem B, Bouchaud E et al (1997) *Phys Rev Lett* 78:1062

## BIOGRAPHICAL SKETCH

Robert Lee Smith was born in the city of Chicago to Robert and Loleta Smith. After graduating from high school, Robert attended Wright State University in Dayton, Ohio for his undergraduate studies where he earned his bachelor's degree in materials science and engineering in 2002. While at Wright State, Robert worked for several years as a co-op in the Materials and Manufacturing Directorate of the Air Force Research Laboratory at Wright-Patterson Air Force Base. He worked on several projects involving the study of metal matrix composites and bulk metallic glasses.

Finished with his undergraduate studies, Robert had the opportunity to move to New Mexico before going to graduate school. He was offered an internship at Los Alamos National Laboratory, where he worked under Carol Haertling and fellow UF alum Robert Hanrahan Jr. While at Los Alamos, Robert was elected president of the Los Alamos Student Association.

At the conclusion of his internship, Robert entered the University of Florida in Gainesville to earn his PhD in materials science and engineering. Robert worked under the guidance of Dr. John J. Mecholsky Jr. During his graduate studies at UF, Robert received several fellowships including the GEM Fellowship and the NSF/SEGEP Fellowship. Taking advantage of the flexible schedule of graduate school, Robert travelled the globe visiting countries like China, Brazil, England, and Germany. In between his many trips, Robert earned his master's degree in materials science in 2006 and his PhD in 2009.